

Impact of beam far side-lobe knowledge in the presence of foregrounds for LiteBIRD

C. Leloup,^{1,2} G. Patanchon,² J. Errard,² C. Franceschet,^{3,4}
 J. E. Gudmundsson,⁵ S. Henrot-Versillé,⁶ H. Imada,⁷ H. Ishino,⁸
 T. Matsumura,¹ G. Puglisi,^{9,10,11} W. Wang,² A. Adler,⁵ J. Aumont,¹²
 R. Aurlien,¹³ C. Baccigalupi,^{14,15,16} M. Ballardini,^{17,18,19}
 A. J. Banday,¹² R. B. Barreiro,²⁰ N. Bartolo,^{21,22,23} A. Basyrov,¹³
 M. Bersanelli,^{3,4} D. Blinov,^{24,25} M. Bortolami,^{17,18} T. Brinckmann,¹⁷
 P. Campeti,^{26,27,18} A. Carones,^{28,29} F. Carralot,¹⁴ F. J. Casas,²⁰
 K. Cheung,^{30,31,32,33} L. Clermont,³⁴ F. Columbro,^{35,36} G. Conenna,³⁷
 A. Coppolecchia,^{35,36} F. Cuttaia,¹⁹ G. D'Alessandro,^{35,36}
 P. de Bernardis,^{35,36} T. de Haan,^{38,39} M. De Petris,^{35,36}
 S. Della Torre,⁴⁰ P. Diego-Palazuelos,^{26,41} H. K. Eriksen,¹³
 F. Finelli,^{19,42} U. Fuskeland,¹³ G. Galloni,²⁸ M. Galloway,¹³
 M. Georges,³⁴ M. Gerbino,¹⁸ M. Gervasi,^{37,40}
 R. T. Génova-Santos,^{43,44} T. Ghigna,³⁹ S. Giardiello,⁴⁵
 C. Gimeno-Amo,²⁰ E. Gjerløw,¹³ A. Gruppuso,^{19,42}
 M. Hazumi,^{39,38,46,1,47} L. T. Hergt,⁴⁸ D. Herranz,²⁰ E. Hivon,⁴⁹
 T. D. Hoang,¹ B. Jost,¹ K. Kohri,³⁸ N. Krachmalnicoff,^{14,15,16}
 A. T. Lee,^{50,31,39} M. Lembo,¹⁷ F. Levrier,⁵¹ A. I. Lonappan,²⁸
 M. López-Caniego,^{52,53} J. Macias-Perez,⁵⁴ E. Martínez-González,²⁰
 S. Masi,^{35,36} S. Matarrese,^{21,22,23,55} S. Micheli,³⁵ M. Monelli,²⁶
 L. Montier,¹² G. Morgante,¹⁹ B. Mot,¹² L. Mousset,^{51,12}
 T. Namikawa,¹ P. Natoli,^{17,18} A. Novelli,³⁵ F. Noviello,⁴⁵ I. Obata,¹
 K. Odagiri,⁴⁶ L. Pagano,^{17,18,56} A. Paiella,^{35,36} D. Paoletti,^{19,42}
 G. Pascual-Cisneros,²⁰ V. Pavlidou,^{24,25} F. Piacentini,^{35,36}
 G. Piccirilli,²⁸ G. Pisano,³⁵ G. Polenta,⁵⁷ N. Raffuzzi,¹⁷
 M. Remazeilles,^{20,30} A. Ritacco,^{58,51} A. Rizzieri,² M. Ruiz-Granda,^{20,41}
 Y. Sakurai,^{8,1} M. Shiraishi,⁵⁹ S. L. Stever,^{8,1} Y. Takase,⁸
 K. Tassis,^{24,25} L. Terenzi,¹⁹ K. L. Thompson,^{60,61} M. Tristram,⁶
 L. Vacher,¹⁴ P. Vielva,²⁰ I. K. Wehus,¹³ G. Weymann-Despres,⁶
 M. Zannoni,^{37,40} and Y. Zhou³⁹
 LiteBIRD Collaboration.

- ¹Kavli Institute for the Physics and Mathematics of the Universe (Kavli IPMU, WPI), UTIAS, The University of Tokyo, Kashiwa, Chiba 277-8583, Japan
- ²Université de Paris, CNRS, Astroparticule et Cosmologie, F-75013 Paris, France
- ³Dipartimento di Fisica, Università degli Studi di Milano, Via Celoria 16 - 20133, Milano, Italy
- ⁴INFN Sezione di Milano, Via Celoria 16 - 20133, Milano, Italy
- ⁵The Oskar Klein Centre, Department of Physics, Stockholm University, SE-106 91 Stockholm, Sweden
- ⁶Université Paris-Saclay, CNRS/IN2P3, IJCLab, 91405 Orsay, France
- ⁷National Astronomical Observatory of Japan, Mitaka, Tokyo 181-8588, Japan
- ⁸Okayama University, Department of Physics, Okayama 700-8530, Japan
- ⁹Dipartimento di Fisica e Astronomia, Università degli Studi di Catania, Via S. Sofia, 64, 95123, Catania, Italy
- ¹⁰INAF, Osservatorio Astrofisico di Catania, via S. Sofia 78, I-95123 Catania, Italy
- ¹¹INFN, Sezione di Catania, via S. Sofia 64, I-95123, Catania, Italy
- ¹²IRAP, Université de Toulouse, CNRS, CNES, UPS, (Toulouse), France
- ¹³Institute of Theoretical Astrophysics, University of Oslo, Blindern, Oslo, Norway
- ¹⁴International School for Advanced Studies (SISSA), Via Bonomea 265, 34136, Trieste, Italy
- ¹⁵INFN Sezione di Trieste, via Valerio 2, 34127 Trieste, Italy
- ¹⁶IFPU, Via Beirut, 2, 34151 Grignano, Trieste, Italy
- ¹⁷Dipartimento di Fisica e Scienze della Terra, Università di Ferrara, Via Saragat 1, 44122 Ferrara, Italy
- ¹⁸INFN Sezione di Ferrara, Via Saragat 1, 44122 Ferrara, Italy
- ¹⁹INAF - OAS Bologna, via Piero Gobetti, 93/3, 40129 Bologna, Italy
- ²⁰Instituto de Física de Cantabria (IFCA, CSIC-UC), Avenida los Castros SN, 39005, Santander, Spain
- ²¹Dipartimento di Fisica e Astronomia “G. Galilei”, Università degli Studi di Padova, via Marzolo 8, I-35131 Padova, Italy
- ²²INFN Sezione di Padova, via Marzolo 8, I-35131, Padova, Italy
- ²³INAF, Osservatorio Astronomico di Padova, Vicolo dell’Osservatorio 5, I-35122, Padova, Italy
- ²⁴Institute of Astrophysics, Foundation for Research and Technology-Hellas, Vasilika Vouton, GR-70013 Heraklion, Greece
- ²⁵Department of Physics and ITCP, University of Crete, GR-70013, Heraklion, Greece
- ²⁶Max Planck Institute for Astrophysics, Karl-Schwarzschild-Str. 1, D-85748 Garching, Germany
- ²⁷Excellence Cluster ORIGINS, Boltzmannstr. 2, 85748 Garching, Germany
- ²⁸Dipartimento di Fisica, Università di Roma Tor Vergata, Via della Ricerca Scientifica, 1, 00133, Roma, Italy
- ²⁹INFN Sezione di Roma2, Università di Roma Tor Vergata, via della Ricerca Scientifica, 1, 00133 Roma, Italy
- ³⁰Jodrell Bank Centre for Astrophysics, Alan Turing Building, Department of Physics and Astronomy, School of Natural Sciences, The University of Manchester, Oxford Road, Manchester M13 9PL, UK
- ³¹University of California, Berkeley, Department of Physics, Berkeley, CA 94720, USA
- ³²University of California, Berkeley, Space Sciences Laboratory, Berkeley, CA 94720, USA
- ³³Lawrence Berkeley National Laboratory (LBNL), Computational Cosmology Center, Berkeley, CA 94720, USA
- ³⁴Centre Spatial de Liège, Université de Liège, Avenue du Pré-Aily, 4031 Angleur, Belgium
- ³⁵Dipartimento di Fisica, Università La Sapienza, P. le A. Moro 2, Roma, Italy
- ³⁶INFN Sezione di Roma, P.le A. Moro 2, 00185 Roma, Italy
- ³⁷University of Milano Bicocca, Physics Department, p.zza della Scienza, 3, 20126 Milan Italy
- ³⁸Institute of Particle and Nuclear Studies (IPNS), High Energy Accelerator Research Organization (KEK), Tsukuba, Ibaraki 305-0801, Japan

- ³⁹International Center for Quantum-field Measurement Systems for Studies of the Universe and Particles (QUP), High Energy Accelerator Research Organization (KEK), Tsukuba, Ibaraki 305-0801, Japan
- ⁴⁰INFN Sezione Milano Bicocca, Piazza della Scienza, 3, 20126 Milano, Italy
- ⁴¹Dpto. de Física Moderna, Universidad de Cantabria, Avda. los Castros s/n, E-39005 Santander, Spain
- ⁴²INFN Sezione di Bologna, Viale C. Berti Pichat, 6/2 – 40127 Bologna Italy
- ⁴³Instituto de Astrofísica de Canarias, E-38200 La Laguna, Tenerife, Canary Islands, Spain
- ⁴⁴Departamento de Astrofísica, Universidad de La Laguna (ULL), E-38206, La Laguna, Tenerife, Spain
- ⁴⁵School of Physics and Astronomy, Cardiff University, Cardiff CF24 3AA, UK
- ⁴⁶Japan Aerospace Exploration Agency (JAXA), Institute of Space and Astronautical Science (ISAS), Sagamihara, Kanagawa 252-5210, Japan
- ⁴⁷The Graduate University for Advanced Studies (SOKENDAI), Miura District, Kanagawa 240-0115, Hayama, Japan
- ⁴⁸Department of Physics and Astronomy, University of British Columbia, 6224 Agricultural Road, Vancouver BC, V6T1Z1, Canada
- ⁴⁹Institut d’Astrophysique de Paris, CNRS/Sorbonne Université, Paris France
- ⁵⁰Lawrence Berkeley National Laboratory (LBNL), Physics Division, Berkeley, CA 94720, USA
- ⁵¹Laboratoire de Physique de l’École Normale Supérieure, ENS, Université PSL, CNRS, Sorbonne Université, Université de Paris, 75005 Paris, France
- ⁵²Aurora Technology for the European Space Agency, Camino bajo del Castillo, s/n, Urbanización Villafranca del Castillo, Villanueva de la Cañada, Madrid, Spain
- ⁵³Universidad Europea de Madrid, 28670, Madrid, Spain
- ⁵⁴Université Grenoble Alpes, CNRS, LPSC-IN2P3, 53, avenue des Martyrs, 38000 Grenoble, France
- ⁵⁵Gran Sasso Science Institute (GSSI), Viale F. Crispi 7, I-67100, L’Aquila, Italy
- ⁵⁶Université Paris-Saclay, CNRS, Institut d’Astrophysique Spatiale, 91405, Orsay, France
- ⁵⁷Space Science Data Center, Italian Space Agency, via del Politecnico, 00133, Roma, Italy
- ⁵⁸INAF, Osservatorio Astronomico di Cagliari, Via della Scienza 5, 09047 Selargius, Italy
- ⁵⁹Suwa University of Science, Chino, Nagano 391-0292, Japan
- ⁶⁰SLAC National Accelerator Laboratory, Kavli Institute for Particle Astrophysics and Cosmology (KIPAC), Menlo Park, CA 94025, USA
- ⁶¹Stanford University, Department of Physics, CA 94305-4060, USA

E-mail: clement.leloup@ipmu.jp

Abstract. We present a study of the impact of a beam far side-lobe lack of knowledge on the measurement of the Cosmic Microwave Background B -mode signal at large scale. Beam far side-lobes induce a mismatch in the transfer function of Galactic foregrounds between the dipole and higher multipoles which degrades the performances of component separation methods. This leads to foreground residuals in the CMB map. It is expected to be one of the main source of systematic effects in future CMB polarization observations. Thus, it becomes crucial for all-sky survey missions to take into account the interplays between beam systematic effects and all the data analysis steps. *LiteBIRD* is the ISAS/JAXA second strategic large-class satellite mission and is dedicated to target the measurement of CMB primordial B modes by reaching a sensitivity on the tensor-to-scalar ratio r of $\sigma(r) \leq 10^{-3}$ assuming $r = 0$. The primary goal of this paper is to provide the methodology and develop the framework to carry out the end-to-end study of beam far side-lobe effects for a space-borne CMB experiment. We introduce uncertainties in the beam model, and propagate the beam effects through all the steps of the analysis pipeline, most importantly including component separation, up to the cosmological results in the form of a bias δr . As a demonstration of our framework, we derive requirements on the calibration and modeling for the *LiteBIRD*’s beams under given assumptions on design, simulation, component separation method and allocated error budget. In particular, we

assume a parametric method of component separation with no mitigation of the far side-lobes effect at any stage of the analysis pipeline.

We show that δr is mostly due to the integrated fractional power difference between the estimated beams and the true beams in the far side-lobes region, with little dependence on the actual shape of the beams, for low enough δr . Under our set of assumptions, in particular considering the specific foreground cleaning method we used, we find that the integrated fractional power in the far side-lobes should be known at the level of $\sim 10^{-4}$, to achieve the required limit on the bias $\delta r < 1.9 \times 10^{-5}$. The framework and tools developed for this study can be easily adapted to provide requirements under different design, data analysis frameworks and for other future space-borne experiments, such as PICO or CMB-Bharat. We further discuss the limitations of this framework and potential extensions to circumvent them.

Contents

1	Introduction	1
2	Overview of <i>LiteBIRD</i>	2
3	Methodology	5
3.1	Simulation of the effect of imperfect beam knowledge	5
3.1.1	Perturbation Case	5
3.1.2	Modeling Case	11
3.2	Component separation	13
3.2.1	Spectral parameters estimation	13
3.2.2	Impact on cosmological results	14
4	Results	15
4.1	Requirements for the Perturbation Case	15
4.1.1	Bias on the tensor-to-scalar ratio from the beam perturbation	15
4.1.2	Beam perturbation power	17
4.1.3	Average perturbation amplitude in the window	18
4.1.4	Noise limited calibration measurements	21
4.2	Requirements for the Modeling Case	22
4.2.1	Comparison of the Detailed Method and the Axisymmetric Method	22
4.2.2	Bias on the tensor-to-scalar ratio from beam mismodeling at large angle	24
5	Discussions	26
5.1	Requirements on calibration	28
5.2	Requirements on modelisation	30
5.3	Limitations, assumptions and future improvements	30
5.4	Application to a realistic physical effect: Ruze’s lobes	32
5.5	Linking requirements to reconstructed beam error bars	32
6	Conclusion	33
7	Acknowledgements	34
A	Correction by the effective beam	36

1 Introduction

Observations of the Cosmic Microwave Background (CMB) radiation have played a crucial role in establishing the concordance model of cosmology in the past 50 years. In particular, data from a sequence of space missions (COBE [1], WMAP [2] and Planck [3]) significantly improved our knowledge of the history of the Universe and its constituents. However, we have yet to probe the imprint of primordial gravitational waves in the curl component of the CMB polarized signal, the so called B modes, which would constitute strong evidence of the hypothetical inflationary period [4–8]. CMB polarization is sourced by scalar, produced by primordial density fluctuations, and tensor perturbations, whose primordial contribution comes exclusively from gravitational waves in the early Universe. The relative amplitude between tensor and scalar modes is captured by the tensor-to-scalar ratio parameter r . A precise measurement of r would allow us to shed new light on the physics of the early Universe and constrain, in particular, the multitude of inflation models. Currently, the best constraint on the tensor-to-scalar ratio is $r < 0.032$ (95% C.L. interval) using a combination of data from the Planck mission and the BICEP/Keck experiment [9].

One of the main challenges in the precision primordial B-mode search is to distinguish between primordial B modes from the inflationary period, and residuals from foreground polarized emissions of our own Galaxy as well as from instrumental systematic effects. A standard method to differentiate the sources is to observe the sky over a broad frequency range and make use of the fact that CMB and Galactic polarized emissions have a different spectral behaviour.

Imperfect knowledge of the optical response of a telescope, its so-called beam pattern, is one of the key systematic effects to be understood in order to properly process the large angular scale signal. In particular, the far side-lobes region at large angle can be very challenging to model and to measure. A number of studies have been carried out to understand the beam systematic effects propagating to observations of past CMB experiments and to evaluate the potential impacts on the scientific outcomes (e.g. in Planck [10–12]). In the context of ground based experiments, e.g. the Atacama Cosmology Telescope or the Simons Observatory, Gallardo et al. [13] addressed the systematic effects in the beam parameters including side-lobe pick-up.

LiteBIRD [14, 15] is the second ISAS/JAXA strategic large-class mission. It will conduct a full-sky survey and measure precisely the polarization anisotropies of the CMB, with a combined sensitivity including statistical errors, foreground residuals and systematic uncertainties on the tensor-to-scalar ratio of $\sigma(r) \leq 0.001$, assuming $r = 0$. *LiteBIRD* will observe the sky in 15 frequency bands from 34 to 448 GHz, with an effective polarization sensitivity of $2.2 \mu\text{K-arcmin}$ and angular resolution ranging from 71 to 18 arcmin, allowing access to multipoles in the range $2 \leq \ell \leq 200$, which will provide unique power to distinguish primordial B modes from the foreground and gravitational weak-lensing B modes. To achieve such a challenging scientific requirement, we need to evaluate the impact of instrumental systematic effects and impose strict requirements on their control. For a reliable estimation of these effects, one has to bridge the science goal and the instrumental specifications, which requires the implementation of various steps, e.g. instrument modeling, sky modeling, and component separation. While a number of studies address some of these steps, to our knowledge none made this bridge fully end-to-end [12, 13, 16–19]. The following work proposes to set up a general framework to study beam systematic effects from the instrumental beam simulations all the way up to their impact on the tensor-to-scalar ratio, which we applied to the particular case of *LiteBIRD* [15]. This allows us to evaluate the required knowledge of instrumental beam to achieve the scientific goal of *LiteBIRD*, in the current experimental context as a first step towards future, more refined study cases. This framework makes use of computational approximations, physical assumptions and arbitrary choices that can impact these requirements. Most notably, the results depend on assumptions on the optical design, approximations for the convolution of the sky with the beams, and the choice of component separation method as well as the allocated error budget for this systematic effect. However, these assumptions can be changed and refined with minimal modifications to the analysis pipeline.

The paper is organized as follows. In Section 2 we describe *LiteBIRD*'s instrumental characteristics relevant for this study. The analysis procedure, detailed in Section 3, is divided into two different approaches depending on the region of the beam under study. The first region, closer to the beam axis, will be accessible to measurements during calibration on the ground and in flight and its knowledge will therefore be impacted by measurement uncertainties. By assessing their impact on cosmological results, compared with the scientific goal of *LiteBIRD*, we can set requirements on the accuracy of these calibration measurements. On the other hand, the second region, further from the beam axis, will be out of reach for precise direct measurements and will rely mostly on modeling combined with indirect measurements. We want to investigate the impact of these modeling uncertainties and the ideal location of the transition between the two regions in order to meet the requirements. These results are presented in Section 4, and their interpretations and limitations are given in Section 5.

2 Overview of *LiteBIRD*

The *LiteBIRD* satellite includes three telescopes at low, medium, and high frequencies (LFT [20], MFT and HFT [21]). With an aperture diameter of 400 mm and an angular resolution ranging from 71 to 24 arcmin, the LFT includes nine frequency bands, three of them redundant making twelve channels within the LFT, distributed from the lower bound of the lowest frequency channel at 34 GHz to the

	ν (GHz)	$\Delta\nu$ ($\Delta\nu/\nu$) (GHz)	Beam size (arcmin)	Number of bolometers	Sensitivity (μ K-arcmin)
LFT	40	12 (0.30)	70.5	48	37.42
	50	15 (0.30)	58.5	24	33.46
	60	14 (0.23)	51.1	48	21.31
	68	16 (0.23)	41.6	144	19.91
			47.1	24	31.77
	78	18 (0.23)	36.9	144	15.55
			43.8	48	19.13
	89	20 (0.23)	33.0	144	12.28
			41.5	24	28.77
100	23 (0.23)	30.2	144	10.34	
119	36 (0.30)	26.3	144	7.69	
140	42 (0.30)	23.7	144	7.25	
MFT	100	23 (0.23)	37.8	366	8.48
	119	36 (0.30)	33.6	488	5.70
	140	42 (0.30)	30.8	366	6.38
	166	50 (0.30)	28.9	488	5.57
	195	59 (0.30)	28.0	366	7.05
HFT	195	59 (0.30)	28.6	254	10.50
	235	71 (0.30)	24.7	254	10.79
	280	84 (0.30)	22.5	254	13.80
	337	101 (0.30)	20.9	254	21.95
	402	92 (0.23)	17.9	338	47.45
Total				4508	2.16

Table 1: *LiteBIRD* specifications in its 22 frequency channels, from [22]. From left to right the columns are: the telescope covering the band, the band center frequency in GHz, the bandwidth in GHz and its ratio to the central frequency, the main beam FWHM in arcmin, the number of bolometers for each channel and the sensitivity in μ K-arcmin.

upper bound of the highest frequency channel at 161 GHz, in order to cover the spectral domains of both CMB and low frequency Galactic emission. Its optical design follows a crossed-Dragone configuration, with a rotating Half-Wave Plate (HWP) as its first optical component. The LFT focal plane is made of tri-chroic lens-coupled Transition Edge Sensors (TES) detectors cooled down to 100 mK. On the other hand, the MFT and HFT, spanning from 89 to 448 GHz, consist of two fully refractive telescopes held on a single mechanical structure, and so are part of a common system called the MHFT. The frequency bands of the MFT range from 89 to 224 GHz, and the HFT from 166 to 448 GHz, with an angular resolution between 18 and 38 arcmin. Therefore, *LiteBIRD* is composed of 15 frequency bands, which partially overlap each other. As a result, the total of 22 frequency channels are distributed from 34 to 448 GHz. Their main characteristics (bands, beam sizes, sensitivities, etc.) are detailed in Table 1. Figure 1 shows the integration of the LFT, MFT and HFT on the *LiteBIRD* satellite [20, 21].

The *LiteBIRD* main scientific requirement $\sigma(r) < 0.001$, assuming $r = 0$, is very challenging from the instrumental point of view. It requires an unprecedented sensitivity at the largest scales and an extreme control of systematic effects. In particular, a good characterization of the beams is of utmost importance as this has a major impact on the quality of observed data. Following the successful NASA WMAP and ESA Planck experiences, the telescope’s main-beam response will be calibrated using the planets [12, 16, 23, 24]. Although some information about the near and far side-lobes can be obtained in flight using planets and brighter objects such as the Moon, such methods face strong limitations. Therefore, most of the knowledge of the side-lobes response typically rely on

a mathematical model validated by the telescope characterization on the ground prior to the launch. Note that we call side-lobes the region of the beam pattern at angles $\gtrsim 5^\circ$ away from the beam axis given the optical system of *LiteBIRD*. The side-lobes characterization of a cryogenically cooled telescope at a millimeter-wave range is known to be challenging. A modeling based performance forecast is also computationally expensive. As a result, it is essential to study the needed accuracy of calibration measurements of the beam side-lobes at an early phase of the project to plan effectively the calibration strategy of *LiteBIRD*.

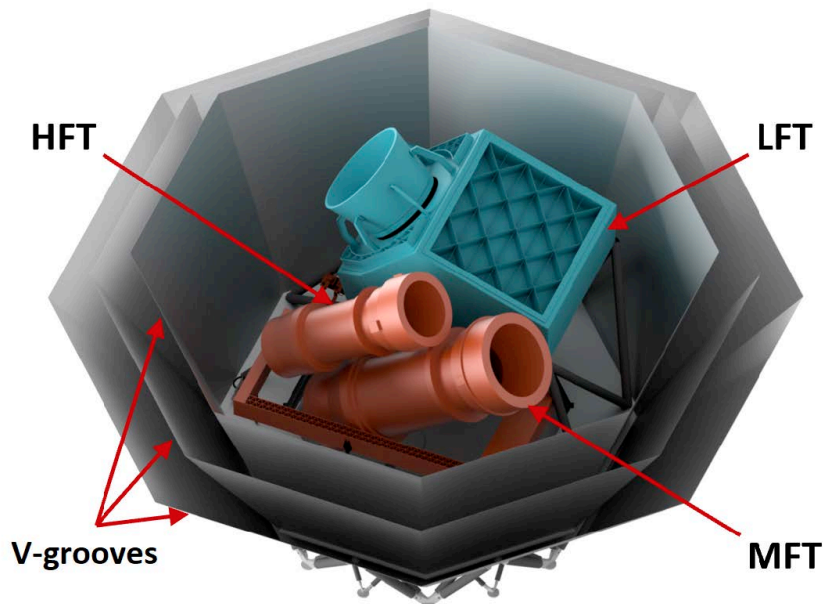


Figure 1: Integration of the three telescopes, the LFT, the MFT and the HFT, to the payload of *LiteBIRD*. The LFT follows a crossed-Dracone design while the MFT and HFT, mounted on the same mechanical structure, are fully refractive telescopes.

The current *LiteBIRD* beam model is based on simulations of the beam response of individual detectors at the center frequency of the frequency bands with GRASP [25], a software tool based on several electromagnetic methods (Physical Optics and Physical Theory of Diffraction, Method of Moments, etc.) accounting for the optical elements expected for each camera deployed in. Given the level of complexity, GRASP simulations have been performed on a smaller set of detectors on the focal planes at this stage, leaving their complete description for future work. For a given pixel in the focal plane, if the GRASP simulation is not available, we consider the closest one (in terms of distance from the axis) and rotate the beam map accordingly to the detector location. Our current GRASP models of the LFT and MHFT telescopes include most of the elements of the nominal optics design, which directly contribute to the response in the main beam region. However, they also include approximations, so they are far from being exhaustive in predicting the radiation pattern at larger angles, in the far side-lobes region, over the whole 4π solid angle. This is particularly true for the LFT model [20]. The MHFT model (see Fig. 2) includes the nominal optical elements of the two refractive telescopes, from the focal plane to the aperture towards the sky: the beam former (a lenslet coupled to sinuous antenna for MFT and a spline-profiled horn for HFT), the two Ultra High Molecular Weight Polyethylene (UHMW-PE) dielectric lenses, the aperture stop of the telescope and a perfectly absorbing fore-baffle. A half-wave plate will be used at the vicinity of the aperture, but is not included in the current beam modeling simulations because of the complexity of its integration.

These elements do not directly contribute to most of the asymmetries in the far side-lobes region of the beam, which are mainly due to the impact of the large mechanical structures of the satellite on the beam (V-grooves, structural elements, etc.) that are not taken into account, but include asymmetries for off-center detectors in the focal plane. A more realistic impact of asymmetries is left for future work.

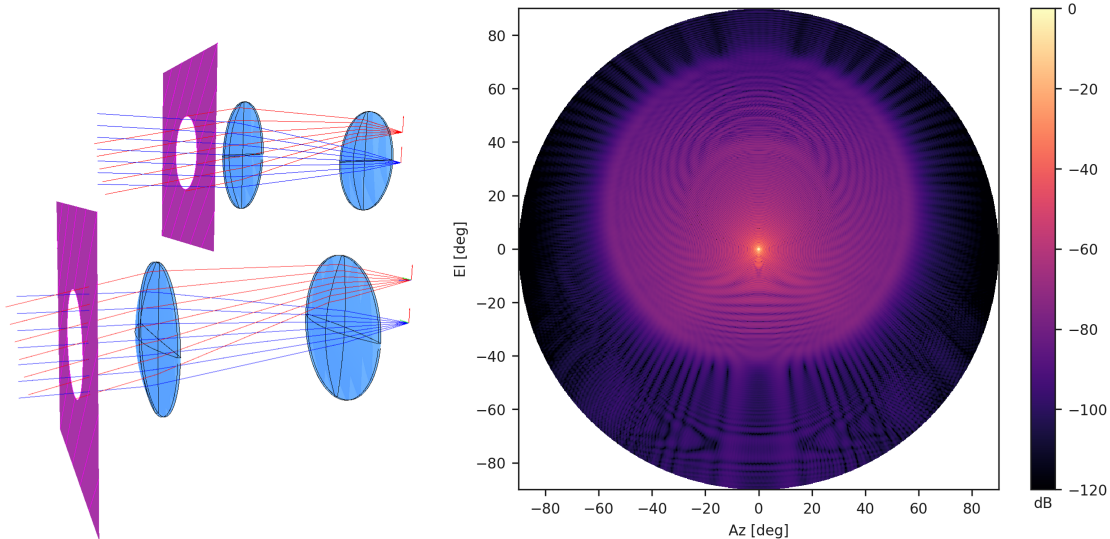


Figure 2: Left: Ray diagrams of MFT (bottom) and HFT (top) models, as implemented into GRASP. The on-axis and edge pixel fields (14 deg) are the blue and red rays, respectively. Right: A full 2π far field beam map (normalized to peak amplitude) for a 100 GHz detector located at the edge of the focal plane.

3 Methodology

3.1 Simulation of the effect of imperfect beam knowledge

In order to study errors arising from an inaccurate knowledge of the beam patterns, we have to simulate the effect of uncertainties on these shapes. We use two distinct approaches to study two different cases. The first approach consists in introducing a localized perturbation of the beam amplitude to account for either statistical or systematic measurement uncertainties during calibration. The second approach relies entirely on a model to estimate the beam shape for angles larger than an angle θ_{lim} , this would correspond to the case where known systematic effects during calibration prevent us from measuring accurately the beam shape at very large angle. In the following, we will refer to the former as the Perturbation Case and to the latter as the Modeling Case. We treat these two approaches separately in Sections 3.1.1 and 3.1.2 respectively, and the general procedure is schematically described in Figure 3.

3.1.1 Perturbation Case

Beam convolution of the sky

We use PySM [26] to simulate the Galactic microwave emission accounting for thermal dust, synchrotron, Anomalous Microwave Emission (AME), free-free, respectively the `d0,s0,a1,f1` models¹. We further include the emission of radio sources both in intensity and polarization following the

¹These refer to models of dust, synchrotron, AME and free-free foreground emissions respectively, with homogeneous spectral energy densities (SEDs) over the sky. AME and free-free are not polarized but are needed in the dipole calibration step where temperature maps are used, see Section 3.1.1.

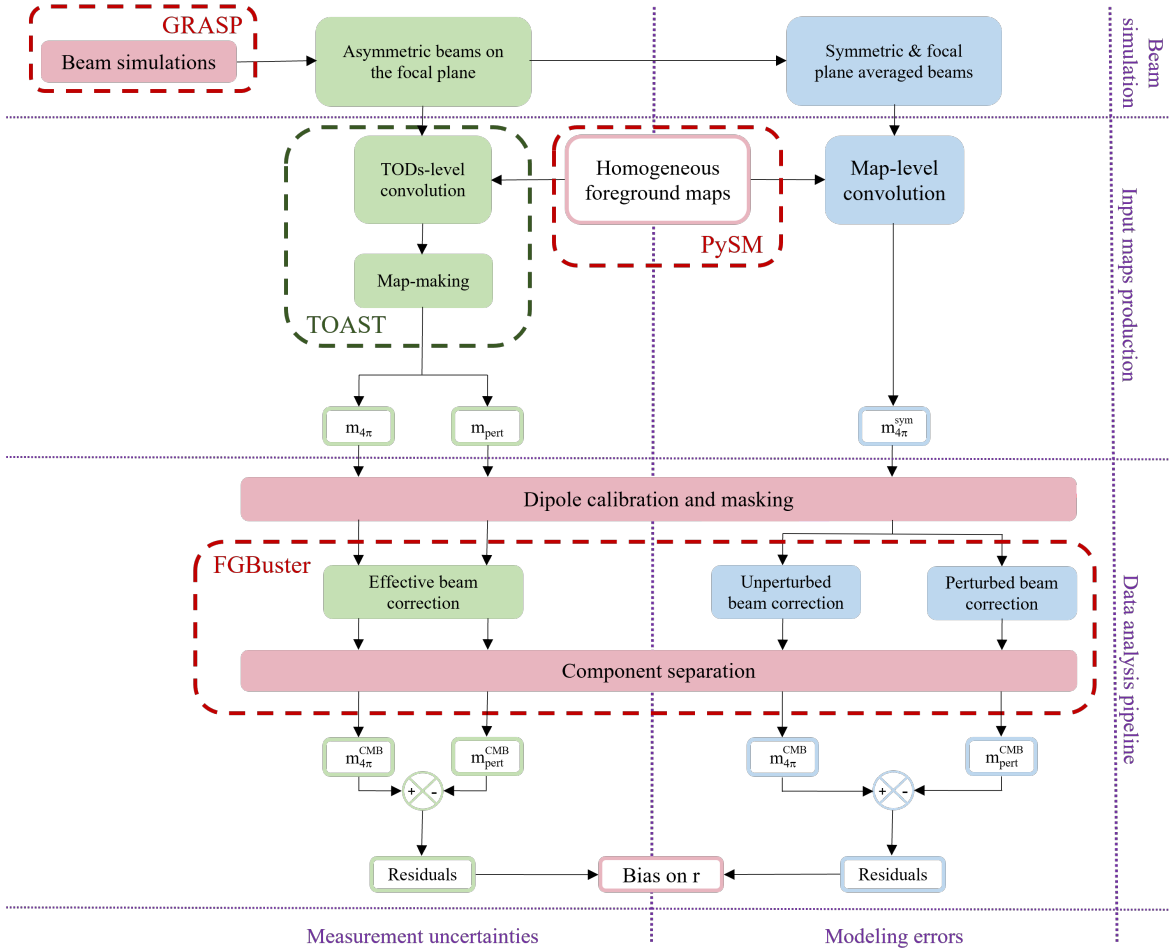


Figure 3: Block diagram summarizing the main analysis steps described in Section 3 to estimate the bias on the tensor-to-scalar ratio, defined as the measured r assuming its true value to be $r_{\text{true}} = 0$, from an uncertainty on the beam shape. In all cases, the perturbed maps (\mathbf{m}_{pert}) include a convolution with perturbed beams while unperturbed maps ($\mathbf{m}_{4\pi}$) are convolved with a reference unperturbed beam. The comparison of the reconstructed CMB maps in these two cases are interpreted as systematic residuals and used to compute δr . Sections 3.1.1 and 3.1.2 describe two different methods, using different definitions of perturbed and unperturbed maps, the former (in green) being more realistic while the latter (in blue) is faster and more flexible. The steps in red are common to both methods. We will see in Section 4.2.1 that the two methods give compatible results.

modeling described in [27, 28]. As the goal of this work is to assess the residuals from systematic uncertainties in terms of CMB B modes, we do not include CMB emission nor other systematic effects to better single out the effect. We do not include noise in the simulations, but due to the component separation treatment described in Section 3.2, the impact of noise is taken into account later in the analysis process. Before beam convolution, the signal is integrated across the *LiteBIRD* frequency band (assumed to be a top-hat for all the detectors). Because the beams themselves are simulated only at the center frequency of each channel, this corresponds to assuming the beams to have no frequency dependence, or alternatively the beam at the central frequency to be representative of the band-averaged beam. This will need to be checked in future, more precise studies including the frequency dependence of the beam patterns. We then use the TOAST [29] software to generate the Time-Ordered Data (TOD) with the nominal scanning strategy of *LiteBIRD*, accounting for a portion

of the focal plane detectors: 50% for LFT, 80% for MFT and 90% for HFT. The beam convolution is done by the `convigt` algorithm [30] implemented in `TOAST`.

As mentioned earlier, we have not taken the HWP into account at the step of the beam modeling. For experiments employing a continuously spinning HWP, the presence of these extra-optical components needs to be correctly accounted for at the step of beam convolution in addition to the conventional beam convolution. A methodology to include HWP rotation with beam convolution by adding an extra-dimension in the data-cube was proposed in [31, 32]. Given the required resolution and number of detectors of current and forthcoming CMB experiments, this represents a limiting factor that makes the convolutions almost unfeasible. We thus present here an approximated procedure able to ensure convolution of polarized signal with the realistic beams simulated with `GRASP` in presence of a spinning HWP. The convolution procedure relies on the assumption that the beam employed for the polarized signals, i.e. b^Q and b^U , is assumed to be the same as the unpolarized one, $b^I = \tilde{I}$. By following the notations adopted by [31], we indicate beam maps in terms of the *Stokes* parameters $b^\mu = (\tilde{I}, \tilde{Q}, \tilde{U}, \tilde{V})$:

$$\begin{aligned} b^I &= (\tilde{I}, 0, 0, 0) \\ b^Q &= (0, \tilde{I}, 0, 0) \\ b^U &= (0, 0, \tilde{I}, 0), \end{aligned} \quad (3.1)$$

with \tilde{I} being the total intensity component of the `GRASP` simulated beam. Once we construct the three beam maps b^I, b^Q, b^U , we use the spherical harmonic (SH) transform to expand each map into $b_{\ell m}^X$ with $X = T, E, B$. Based on our assumption (3.1) that there is no $I \rightarrow P$ leakage in our simulations, we have $b_{\ell m}^{I,E} = b_{\ell m}^{I,B} = b_{\ell m}^{Q,T} = b_{\ell m}^{U,T} = 0$.

The transformation in harmonic domain speeds up the convolution step as it becomes a simple product of the $b_{\ell m}^X$ with the SH coefficients of the input sky $a_{\ell m}$. We perform 3 separate convolutions:

1. multiplication in harmonic space of the unpolarized $a_{\ell m}^I$ by the $b_{\ell m}^I$ beam;
2. multiplication in harmonic space of the polarized component $_{-2}a_{\ell m}^P$ by the $_{-2}b_{\ell m}^P$ beam;
3. multiplication in harmonic space of the polarized component $_{2}a_{\ell m}^P$ by the $_{2}b_{\ell m}^P$ beam;

where $a_{\ell m}^I$ and $_{\pm 2}a_{\ell m}^P$ stands for the spherical harmonic coefficients of total intensity and both the *E*-mode and *B*-mode components, respectively. The final convolved TOD is thus [31]:

$$d_t \propto \sum_{\ell m} \sqrt{\frac{4\pi}{2\ell+1}} \left[b_{\ell s}^{I*} a_{\ell m}^I + \frac{1}{2} \left(-_{2}b_{\ell s}^{P*} -_{2}a_{\ell m}^P e^{-4i\phi_t} + {}_2b_{\ell s}^{P*} {}_2a_{\ell m}^P e^{4i\phi_t} \right) \right] e^{-is\psi_t} {}_sY_{\ell m}(\Omega_t), \quad (3.2)$$

with ψ_t being the orientation angle of the detectors at time t and ϕ_t the angle of the HWP at time t . Using Eq. (3.2), we can efficiently separate the data sampling and the convolution into two steps [30], by evaluating the inverse spherical harmonics over the sphere for each azimuthal mode s of the beam. Once the maps are computed, we use the pointing and phase information to sample the TOD d_t . It was shown in [31] that $s_{max} \ll \ell_{max}$ thanks to the azimuthal band-limit of the simulated beam so that each s mode can be independently treated and recursively estimated via $e^{i(s+1)\psi} = e^{is\psi} e^{i\psi}$.

Using this framework, we produce several series of convolutions by applying different apodization functions to the nominal beam patterns to consider the side-lobes contribution only:

$$A(\theta, \theta_{cut}) = \begin{cases} 0 & \text{if } \theta < \theta_{apo} \\ \frac{1}{2} \left(1 - \cos \left(\frac{(2\theta - \theta_{cut})\pi}{\theta_{cut}} \right) \right) & \text{if } \theta_{apo} < \theta < \theta_{cut} \\ 1 & \text{if } \theta_{cut} < \theta, \end{cases} \quad (3.3)$$

where $\theta_{apo} = \theta_{cut}/2$ is the angle at which we start the apodization and θ is defined in $[0^\circ, 180^\circ]$. This axisymmetric apodization is applied to the beam pattern to extract the contribution of the side-lobes starting from the angle θ_{cut} . In this way, we extracted the side-lobes starting from 3 different angular distances ($\theta_{cut} = 5^\circ, 10^\circ, 15^\circ$), producing $\mathbf{m}(\theta > \theta_{cut}) = \mathbf{m}_{cut}$ maps, and the full 4π beam, producing

$\mathbf{m}_{4\pi}$ maps. Note that this is an abusive notation as GRASP produces beam maps only up to $\theta = \pi/2$, so $\mathbf{m}_{4\pi}$ is convolved by a 2π beam, rigorously speaking, and the beam is assumed to vanish for $\theta > \pi/2$. Nevertheless, we will continue using it in the following. The three apodization functions used in the following are illustrated in Figure 4. These three angular ranges are chosen to probe several levels of side-lobe pick-up given the specifics of the *LiteBIRD* optics and the experimental constraints to characterize at high significance level the beam pattern.

We want to emphasize that even though all the specific features related to co-polar components are obtained by GRASP simulations, they are lost from the use of the transformations in Eq. (3.1). Thus, they are not encoded in the convolution and the beam non-idealities (e.g. side-lobe pick up) for the co-polar component are assumed to be similar to the ones from \tilde{I} . Moreover, the results presented here are obtained with an approximated convolution method as the cross-polar component of the beam, albeit small, is totally neglected in the beam decomposition Eq. (3.1). This is mainly supported by the fact that linear polarization detectors are designed to have a minimal cross-polar response, and thus instrumental beams are often approximated in the literature as just co-polar. The derivation of requirements with an implementation properly accounting for cross-polar components of the beam is left for future work.

Perturbed beam maps

The study presented here relies on the production of simulated maps including the generation of sky emissions, map-making and realistic beam convolution in various settings. Given the complexity and time consumption of such simulations, we keep their production to the bare minimum and simulate the effect of an imperfect beam knowledge directly at the map level. Therefore, we combine the previously defined sets of maps \mathbf{m}_{cut} and $\mathbf{m}_{4\pi}$ to produce maps convolved with perturbed beams. By producing the map difference $\mathbf{m}(\theta > \theta_{\text{inf}}) - \mathbf{m}(\theta > \theta_{\text{sup}}) \equiv \mathbf{m}_{\text{inf}} - \mathbf{m}_{\text{sup}}$, we are left with maps that correspond to a convolution of the sky by the beams in the angular region between θ_{inf} and θ_{sup} , i.e. in an angular window function defined as:

$$W(\theta) \equiv A(\theta, \theta_{\text{inf}}) - A(\theta, \theta_{\text{sup}}). \quad (3.4)$$

Throughout this paper, we consider three angular ranges $[\theta_{\text{inf}}, \theta_{\text{sup}}]$: $[5^\circ, 10^\circ]$, $[10^\circ, 15^\circ]$ and $[15^\circ, 180^\circ]$. To be more representative, we describe the angular range spanned by these windows in terms of the angles at half maximum, which are respectively: $[4^\circ, 8^\circ]$, $[7^\circ, 12^\circ]$ and $[11^\circ, 180^\circ]$. The window functions corresponding to these angular ranges can be seen in Figure 4.

We see that, given these three combinations of maps we can select parts of the beam on rings at different angular radial distances from the beam axis, with some small overlap between the three cases. This way, it is possible to generate maps convolved by a perturbed beam, where the perturbation is localized in these annular rings and the shape of the perturbation is that of the nominal beam. These maps are produced using the following combination:

$$\mathbf{m}_{\text{pert}}(\alpha) = \mathbf{m}_{4\pi} + \alpha(\mathbf{m}_{\text{inf}} - \mathbf{m}_{\text{sup}}), \quad (3.5)$$

where α is an arbitrary parameter that drives the amplitude of the beam perturbation, that will be referred to simply as the perturbation amplitude in the following. Note that, because the beam amplitude is a positive quantity, we must have $\alpha \geq -W_{\text{max}}^{-1}$, where W_{max} is the maximum of the window function over the angular range. An example of the perturbed beam profile (averaged over the detectors and symmetrized, see Section 3.1.2) by which $\mathbf{m}_{\text{pert}}(\alpha)$ at 100 GHz in the LFT is convolved, with $\alpha = 2.0$, is given in Figure 5.

Dipole calibration

Since component separation methods are based on the relative comparison of the amplitude of observed maps in the different frequency channels, these maps must be properly normalized beforehand. In particular, the combination of maps described by Eq. (3.5) modifies the map normalization compared to that of $\mathbf{m}_{4\pi}$. Therefore, we need to renormalize these maps before applying component separation. The renormalization is performed by matching the temperature dipoles $C_{\ell=1}^{TT}$ of the perturbed maps

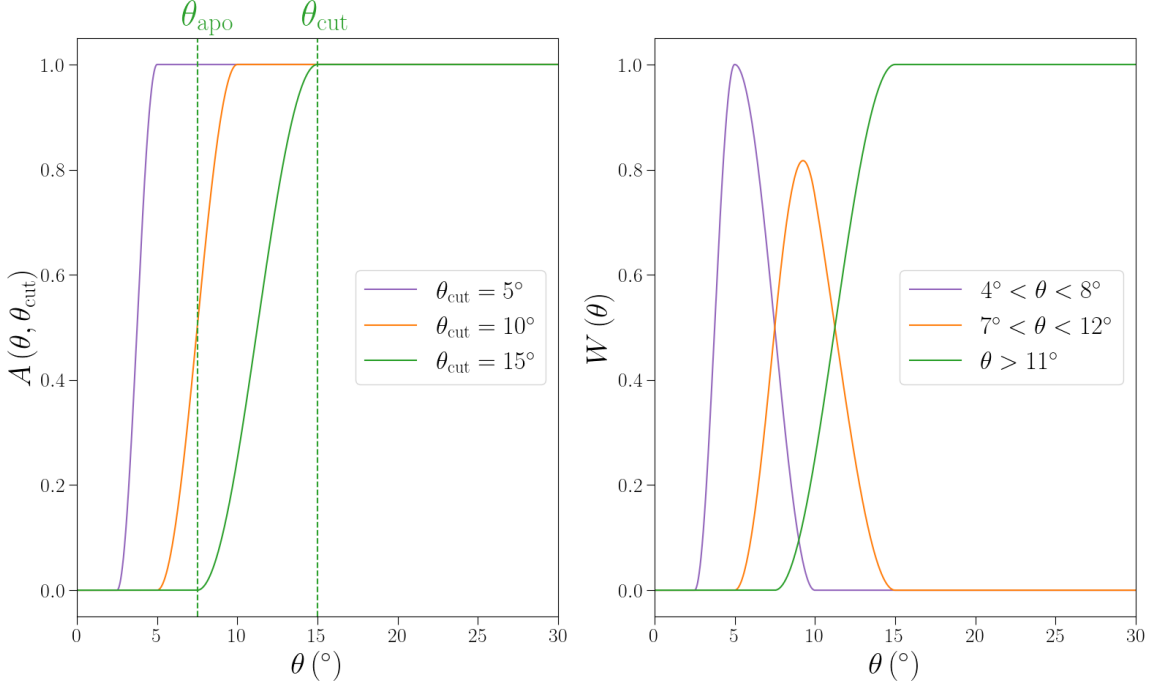


Figure 4: (Left) Apodization functions as defined in Eq. (3.3) for three values of θ_{cut} : 5° , 10° and 15° . The definition of θ_{apo} and θ_{cut} are emphasized for the case $\theta_{\text{cut}} = 15^\circ$. (Right) Beam window functions defined as in Eq. (3.4), for three sets of $[\theta_{\text{inf}}, \theta_{\text{sup}}]$: $[5^\circ, 10^\circ]$, $[10^\circ, 15^\circ]$ and $[15^\circ, 180^\circ]$. The corresponding angular ranges at half maximum are: $[4^\circ, 8^\circ]$, $[7^\circ, 12^\circ]$ and $[11^\circ, 180^\circ]$.

with those of $\mathbf{m}_{4\pi}$. This is equivalent to a perfect calibration of the maps on the dipole, in other words the perturbation of the beam we introduce has no impact on the dipole calibration. This is justified because the procedure of gain calibration on the dipole is entirely decoupled from the beam calibration. In the present work, we want to isolate the effect of imperfect beam knowledge from other systematic effects so the study of a potential coupling with dipole miscalibration, as well as with other systematic effects, is left for future work. For a study of the effect of errors on gain calibration in the context of *LiteBIRD*, see [33].

Using this normalization convention, the maps convolved by a perturbed beam with a normalization factor μ , hereafter the “perturbed maps”, are defined by:

$$\mathbf{m}_{\text{pert}}(\alpha) = \mu [\mathbf{m}_{4\pi} + \alpha (\mathbf{m}_{\text{inf}} - \mathbf{m}_{\text{sup}})], \quad (3.6)$$

After a little algebra, we find the analytical expression for μ to be determined by the dipoles of the relevant maps previously defined:

$$\mu = \sqrt{\frac{C_{\ell=1}^{4\pi}}{C_{\ell=1}^{4\pi} + 2\alpha (C_{\ell=1}^{4\pi-\text{inf}} - C_{\ell=1}^{4\pi-\text{sup}}) + \alpha^2 (C_{\ell=1}^{\text{inf}} - 2C_{\ell=1}^{\text{inf-sup}} + C_{\ell=1}^{\text{sup}})}}, \quad (3.7)$$

where $C_{\ell=1}^X$ is the value of the temperature power-spectrum of X at $\ell = 1$ (4π standing for $\mathbf{m}_{4\pi}$, inf for \mathbf{m}_{inf} and sup for \mathbf{m}_{sup}) and $C_{\ell=1}^{X-Y}$ is the value of the temperature cross-spectrum of X and Y .

Once all these preparation steps are performed, the resulting maps are effectively convolved with the following perturbed beams:

$$B_{\text{pert}}^\nu(\theta, \phi) = \mu_\nu (1 + \alpha_\nu W(\theta)) B_0^\nu(\theta, \phi), \quad (3.8)$$

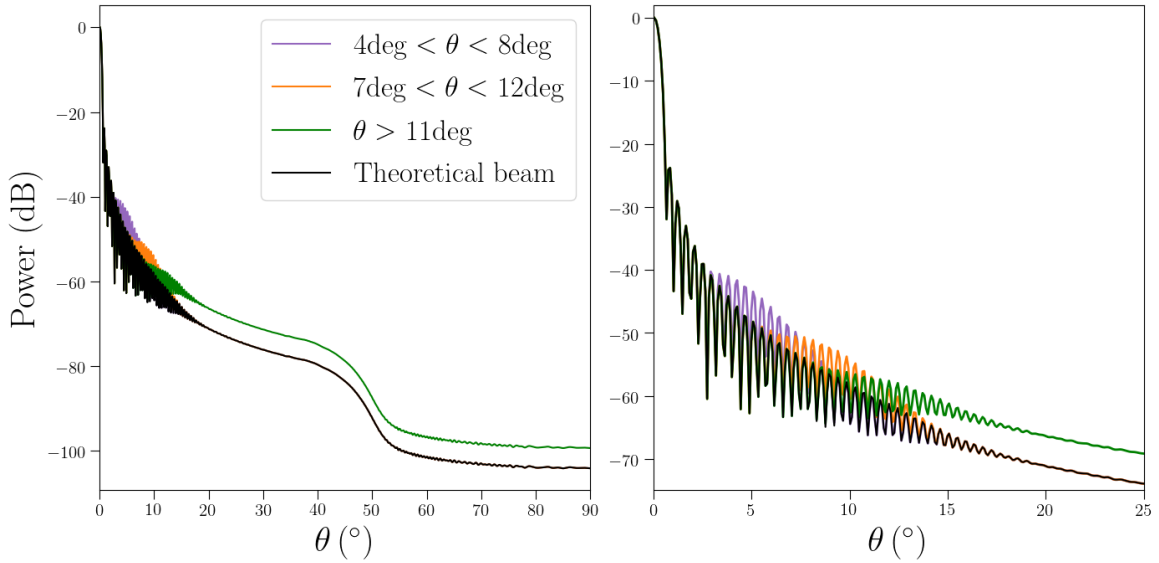


Figure 5: Examples of perturbed beams used in this analysis in *LiteBIRD*'s 100 GHz channel, in the three angular windows [4deg, 8deg] (purple), [7deg, 12deg] (orange) and [11deg, 180deg] (green), compared to the nominal beam (black) used in the convolution of the reference $\mathbf{m}_{4\pi}$ maps, for a perturbation amplitude $\alpha = 2.0$. The left panel shows the whole beam profile while the right panel is zoomed on the $[0^\circ, 25^\circ]$ angular range.

where B_0^ν corresponds to the simulated GRASP beams used to convolve the sky maps in the frequency channel ν .

Beam correction and masking

The observed maps are convolved with the beams. In order to follow the steps of the real analysis pipeline, we deconvolve the observed data in harmonic domain using transfer functions b_ℓ^ν in each frequency band to obtain beam corrected harmonic coefficients $\mathbf{a}_{\ell m, \text{corr}}^\nu$. In the real analysis, these transfer functions would be computed from the beam maps estimated from calibration and modeling. Note that beam asymmetries present in the input beam models are not taken into account in this step, but will not affect the final results as will be explained in Section 3.2. Indeed, we are interested in the effect of imperfect beam knowledge on the cosmological results so we will ultimately compare the contamination in the reconstructed CMB maps from the perturbed ($\mathbf{m}_{\text{pert}}^\nu$) and unperturbed cases ($\mathbf{m}_{4\pi}^\nu$). Therefore, as long as the same $b_{\ell, \text{eff}}^\nu$ are used in the perturbed and unperturbed cases, our results will not depend on the shape of the effective beams. For this reason, we defer the details of the computation of these transfer functions to Appendix A.

The last step needed to produce the input data for the component separation step is to apply a mask to the Galactic plane where the foreground signal is very strong. This amounts to scaling each pixel's amplitude using weights $\mathbf{w} \in [0, 1]$ where \mathbf{w} is 0 in the masked region, and smoothly gets to 1 in the region used for the analysis. Therefore, we first need to translate back the corrected $\mathbf{a}_{\ell m, \text{corr}}$ into pixel amplitudes $\mathbf{m}_{\text{pert}}^{\text{corr}}$ before applying the mask weights:

$$\mathbf{m}_{\text{pert}}^{\text{masked}} = \mathbf{w} \cdot \mathbf{m}_{\text{pert}}^{\text{corr}}. \quad (3.9)$$

This step, in itself, will introduce mixing between the Q and U components leading to $E \rightarrow B$ leakage. However, this should not have a significant impact on residuals from beam far side-lobes systematic mismatch as will be explained in section 3.2. In this study, we used the Planck HFI Galactic mask with $f_{\text{sky}} \sim 51\%$ [34].

Finally, because we use component separation in the harmonic domain, we perform a last translation of maps into harmonic domain, where we are dealing with pseudo- $\mathbf{a}_{\ell m}$'s because of the masking.

3.1.2 Modeling Case

We know that, in a realistic set-up, direct measurements of the beams will be very challenging in the region very far from the center of the beam, and our main estimation of the beam amplitude would be from modeling. We want to study the impact of modeling errors in this region and its dependence in the angle θ_{lim} from which measurements are absent, which constitutes our Modeling Case. We employ a different method, as opposed to the ‘‘Detailed Method’’ presented in Section 3.1.1, referred to as the ‘‘Axisymmetric Method’’, to carry out this study. This is because the Detailed Method that relies on focal plane simulation and TOD level convolution is computationally heavy, which is not well suited for the Modeling Case as we need to explore a broader parameter space (of the order of $\sim 10^4$ configurations) see Section 4.2. As a result, we employ in the Axisymmetric Method a faster and more flexible way of producing beam convolved maps based on an axisymmetric approximation.

It appears clear that the previously described methodology of local perturbation of the beam is also not very well suited for the study of the Modeling Case. We develop in this section a more adapted approach.

Beam convolved map production

The approach developed in Section 3.1.1 is based on extensive simulations of realistic sky maps convolved with perturbed beams including simulations of the focal plane, scanning strategy effects, and taking some level of beam asymmetry into account. In the context of the current section, as we mentioned above, we need a more flexible and quicker procedure. Therefore, we adopt here another similar but simpler approach. The maps are convolved by the same beam in all studied cases, the assumed true beams \overline{B}_0^ν are taken from the simulated GRASP beams B_0^ν by averaging over the simulated detectors of the focal plane and symmetrizing them around the beam axis, i.e. averaging over the ϕ coordinate. On the other hand, they are corrected using the transfer functions corresponding to the assumed beam model of the analysis. In harmonic space, the $\mathbf{a}_{\ell m}$ to be used in component separation are defined as:

$$\mathbf{a}_{\ell m} = \frac{b_\ell^{\text{GRASP}}}{b_\ell^{\text{model}}} \mathbf{a}_{\ell m}^{\text{sky}}, \quad (3.10)$$

with $\mathbf{a}_{\ell m}^{\text{sky}}$ corresponding to simple band-passes integrated foreground maps assuming the spatially homogeneous model d0s0 of PySM [26] and the b_ℓ 's being the transfer functions of the averaged symmetrized GRASP beams and of the beam models. We also apply the same masking scheme. In the same way, we make sure to reproduce the effect of dipole calibration, assumed perfect, by re-scaling the model transfer function such that $b_{\ell=1}^{\text{model}} = b_{\ell=1}^{\text{GRASP}}$.

We will show in Section 4.2.1 that this method relying on the axisymmetric beam approximation and the more realistic one described in Section 3.1.1 gives, in fact, very comparable results in our settings. The interpretation of this correspondence will also be discussed in Section 5.

Beam modeling at large angle

We assume the beam to be perfectly known in the central region, for angles lower than an arbitrary θ_{lim} . For angles $\theta > \theta_{\text{lim}}$, we assume an empirical beam model to simulate the complete lack of information on the true beam shape in this region. As explained earlier, one of the goals of the present study is to estimate angles θ_{lim} for which the induced error from this lack of information is compatible with the scientific goals of the mission. Two conservative empirical models would be a constant amplitude $B_{\text{lim}} = B_{\text{true}}(\theta_{\text{lim}})$, or otherwise to cut the beam for $\theta > \theta_{\text{lim}}$. However, both these two cases are too simplistic and overly pessimistic. In addition, the results obtained by using this kind of empirical model would be very dependent on the assumed true beam used in the analysis.

Therefore, we need a more complex model to capture the essential features, to be determined, of the true beam. The question of how complex the model should be is essential in this analysis since

complexity is at the expense of flexibility and generality. With these considerations in mind, we keep the complexity low and consider simple power laws for $\theta > \theta_{\text{lim}}$ with an arbitrary parameter $b \geq 0$:

$$B_{\text{model}}^{\nu}(\theta, \theta_{\text{lim}}, b) = (1 - A'(\theta, \theta_{\text{lim}})) \overline{B}_0^{\nu} + A'(\theta, \theta_{\text{lim}}) B_{\text{lim}}^{\nu} \left(\frac{\theta_{\text{lim}}}{\theta} \right)^b. \quad (3.11)$$

The function A' is an apodization function, with a much sharper transition than in Eq. (3.3), because it needs to compensate the high amplitude of the power law $B_{\text{lim}}^{\nu} \left(\frac{\theta_{\text{lim}}}{\theta} \right)^b$ at low θ in a large range of possible θ_{lim} . It is taken to be the following logistic function:

$$A'(\theta, \theta_{\text{lim}}) = \frac{1}{1 + e^{20(\theta_{\text{lim}} - \theta)/1^\circ}}. \quad (3.12)$$

The case $b = 0$ in Eq. (3.11) gives back the constant model and the case $b \rightarrow \infty$ leads to the cut beam. Therefore, this model includes the two most non-informative models, but also all the intermediate cases. Examples of such beam models are shown in Figure 6 for several values of b and $\theta_{\text{lim}} = 30^\circ$, in *LiteBIRD*'s LFT 100 GHz channel. We will see in Section 4.2 that these very simple models are enough to grasp the most important characteristic of the beams, i.e. the residual power in the far side-lobes.

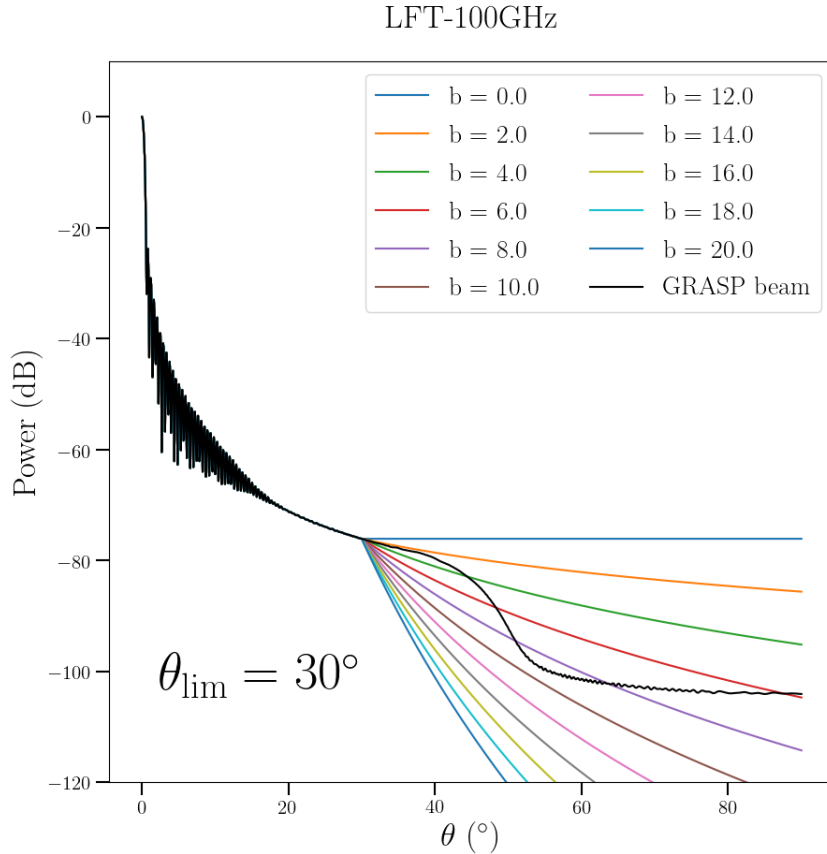


Figure 6: Examples of beam models in *LiteBIRD*'s LFT 100 GHz channel compared to the averaged and symmetrized GRASP beam used as true beam reference. The limit angle is taken to be $\theta_{\text{lim}} = 30^\circ$, and the arbitrary parameters of the power law model is taken to be $b \in [0, 20]$.

3.2 Component separation

3.2.1 Spectral parameters estimation

The goal of component separation for foreground cleaning is to retrieve the CMB and possibly other components emission maps from the observed frequency maps \mathbf{m}^ν . In particular, we are concerned with the contamination from polarized Galactic dust, dominant at high frequencies, and synchrotron, dominant at low frequencies, which are expected to have a significant impact on the scientific results if not properly cleaned [35–37]. Taking the foreground cleaning step into account is very important in this analysis since the main effect of beam miscorrection is to shift the relative amplitude between frequency channels, changing the effective SEDs of the components for multipoles $\ell \geq 2$. The component separation technique used in this analysis is based on the method described in [38, 39] and implemented in the `FGBuster` package, with the notable difference that it operates in harmonic domain. This component separation method is based on a parametric approach where the foreground components spectral properties are modeled using analytic emission laws. The dust component is modeled by a modified black-body law with temperature T_d and spectral parameter β_d , while the synchrotron emission is modeled by a simple power law with spectral parameter β_s . These three parameters are assumed constant over the sky and are fitted using the maximum-likelihood principle. Therefore, this component separation method is based on fitting the SEDs from the relative amplitudes of the frequency maps which are significantly altered for all $\ell \geq 2$ by the dipole calibration of maps with large leakage from the Galactic plane. This makes our approach to foreground cleaning particularly sensitive to the effect of a mismatch in the far side-lobes region.

The observed maps are assumed to be the result of combined emissions from the different sources, CMB and foreground components, together with instrumental noise. Therefore, the observed amplitudes \mathbf{m}_p in a single pixel gathered in a vector of n_ν frequencies are assumed to be produced by n_c components, and is modeled in pixel space as:

$$\mathbf{m}_p = \mathbf{A}(\beta) \mathbf{s}_p + \mathbf{n}_p. \quad (3.13)$$

In the above data model, \mathbf{A} is a matrix that gives each components' amplitude scaling across frequency bands and depends on a set of foreground parameters that we collectively refer to as the spectral parameters β , \mathbf{s}_p is a vector describing the amplitude of the different components in the pixel p , and \mathbf{n}_p is the amplitude of instrumental noise in this pixel assuming white noise determined from the sensitivities in Table 1. These elements have the following dimensions:

$$\mathbf{m}_p, \mathbf{n}_p = \left[\begin{array}{c} \vdots \\ \vdots \end{array} \right] \Bigg\} n_\nu \quad \mathbf{A} = \left[\underbrace{\dots}_{n_c} \right] \Bigg\} n_\nu \quad \mathbf{s}_p = \left[\begin{array}{c} \vdots \\ \vdots \end{array} \right] \Bigg\} n_c. \quad (3.14)$$

Assuming that the noise is Gaussian with covariance matrix \mathbf{N}_p , the log-likelihood for the data given the model is:

$$\mathcal{S} \equiv -2 \ln \mathcal{L} = \text{const} + \sum_p (\mathbf{m}_p - \mathbf{A}\mathbf{s}_p)^T \mathbf{N}_p^{-1} (\mathbf{m}_p - \mathbf{A}\mathbf{s}_p). \quad (3.15)$$

In the following, we drop the constant term as it does not impact the position of the maximum. As mentioned previously, the parameters over which we maximize the likelihood are the foreground spectral parameters β and the amplitudes of the components \mathbf{s} . The vanishing partial derivatives of the likelihood at the maximum imply:

$$-\sum_p \left(\frac{\partial \mathbf{A}}{\partial \beta} \mathbf{s}_p \right)^T \mathbf{N}_p^{-1} (\mathbf{m}_p - \mathbf{A}\mathbf{s}_p) = 0 \quad (3.16)$$

$$\mathbf{s}_p = (\mathbf{A}^T \mathbf{N}_p^{-1} \mathbf{A})^{-1} \mathbf{A}^T \mathbf{N}_p^{-1} \mathbf{m}_p. \quad (3.17)$$

Evaluating the likelihood Eq. (3.15) at the maximum of \mathbf{s}_p , Eq. (3.17) allows us to define the profile likelihood, or spectral likelihood, which depends only on the spectral parameters β :

$$\mathcal{S}_{spec} = - \sum_p \mathbf{m}_p^T \mathbf{N}_p^{-1} \mathbf{A} (\mathbf{A}^T \mathbf{N}_p^{-1} \mathbf{A})^{-1} \mathbf{A}^T \mathbf{N}_p^{-1} \mathbf{m}_p. \quad (3.18)$$

As was pointed out at the end of Section 3.1.1, we work in harmonic domain instead of pixel domain. Therefore, we have to expand \mathbf{m}_p and \mathbf{N}_p on the basis of spherical harmonics. We use the spherical harmonic transform operator $\mathbf{Y}_{\ell m}$ and define the data harmonic coefficients $\mathbf{a}_{\ell m}$ as well as the noise covariance in harmonic domain $\mathcal{N}_{\ell_1 m_1, \ell_2 m_2}$ by the following relations:

$$\mathbf{m}_p = \sum_{\ell, m} \mathbf{Y}_{\ell m, p}^\dagger \mathbf{a}_{\ell m} \quad \text{and} \quad \mathbf{N}_p^{-1} = \sum_{\ell_1, \ell_2, m_1, m_2} \mathbf{Y}_{\ell_1 m_1, p} \mathcal{N}_{\ell_1 m_1, \ell_2 m_2}^{-1} \mathbf{Y}_{\ell_2 m_2, p}^\dagger. \quad (3.19)$$

Given the orthogonality of spherical harmonics on the full sky, that we can use even though we only observe a limited patch of the sky by setting \mathbf{m}_p outside the patch to be zero, the spectral likelihood becomes:

$$\mathcal{S}_{spec} = - \sum \mathbf{a}_{\ell_1 m_1}^\dagger \mathcal{N}_{\ell_1 m_1, L_1 M_1}^{-1} \mathbf{A} \left(\mathbf{A}^T \mathcal{N}_{L_1 M_1, L_2 M_2}^{-1} \mathbf{A} \right)^{-1} \mathbf{A}^T \mathcal{N}_{L_2 M_2, \ell_2 m_2}^{-1} \mathbf{a}_{\ell_2 m_2}, \quad (3.20)$$

where the sum runs over all harmonic indices. If we further assume \mathbf{N}^{-1} to be diagonal in harmonic space, i.e. homogeneous noise, and to depend only on ℓ , the spectral likelihood simplifies to:

$$\mathcal{S}_{spec} = - \sum_{\ell, m} \mathbf{a}_{\ell m}^\dagger \mathcal{N}_\ell^{-1} \mathbf{A} (\mathbf{A}^T \mathcal{N}_\ell^{-1} \mathbf{A})^{-1} \mathbf{A}^T \mathcal{N}_\ell^{-1} \mathbf{a}_{\ell m}. \quad (3.21)$$

Since we are interested in forecasting the impact of beam shape uncertainty on component separation, we only work with the likelihood averaged over noise realizations. Moreover, as detailed in the previous sections, we apply a correction for the beam shape by deconvolving the maps using effective beams b_ℓ^{eff} , therefore the noise covariance matrix is scaled by a factor $(b_\ell^{eff})^{-2}$. The noise averaged spectral likelihood is given by:

$$\langle \mathcal{S}_{spec} \rangle_{noise} = - \sum_{\ell, m} \text{Tr} \left[\mathcal{N}_\ell^{-1} \mathbf{A} (\mathbf{A}^T \mathcal{N}_\ell^{-1} \mathbf{A})^{-1} \mathbf{A}^T \mathcal{N}_\ell^{-1} \left(\hat{\mathbf{a}}_{\ell m} \hat{\mathbf{a}}_{\ell m}^\dagger + \hat{\mathcal{N}}_\ell \right) \right], \quad (3.22)$$

where $\hat{\mathbf{a}}_{\ell m}$ are the true (noiseless) observed multipoles, including only beam convolved foreground emissions, and $\hat{\mathcal{N}}_\ell$ is the true noise covariance. If we assume that $\hat{\mathcal{N}}_\ell = \mathcal{N}_\ell$, this likelihood reduces to the spectral likelihood Eq. (3.21) involving noiseless data, and it was shown in [39] that CMB data does not play any role on the likelihood maximization. This justifies the use of foreground only input maps in this analysis. Note that the likelihood is defined for each Stokes parameter independently, because we assume no leakage from T to P, or from E to B. Indeed, this effect is expected to be mostly mitigated by the HWP, and the residual leakage to be of second order compared to foreground residuals. Therefore, we consider only the CMB B modes in this work.

3.2.2 Impact on cosmological results

By maximizing the spectral likelihood Eq. (3.22), we recover spectral parameters β . These are then used to clean foreground emissions from frequency maps and recover the CMB map. The estimate of the components is given by:

$$\bar{\mathbf{s}}_{\ell m} = (\mathbf{A}^T \mathcal{N}_\ell^{-1} \mathbf{A})^{-1} \mathbf{A}^T \mathcal{N}_\ell^{-1} \hat{\mathbf{a}}_{\ell m}. \quad (3.23)$$

An error on the spectral indices will lead to foreground leakage into CMB maps and larger reconstructed CMB power spectra. The perturbation introduced to account for the uncertainty on the shape of beam far side-lobes can impact the measurement of the spectral parameters, therefore introducing systematic residuals on the CMB B-mode power spectrum and systematic bias δr on the tensor-to-scalar ratio r .

Because we want to disentangle the impact of systematic error from beam shape mismatch and intrinsic systematic errors of the component separation procedure, we define the residuals to be the difference between the recovered CMB B -mode multipoles in a reference case $\bar{\mathbf{s}}_{\ell m}^{\text{ref}}$ that assumes no beam perturbation and the recovered CMB B -mode multipoles in the perturbed case $\bar{\mathbf{s}}_{\ell m}$ (see [15]):

$$\delta \mathbf{s}_{\ell m} = \bar{\mathbf{s}}_{\ell m} - \bar{\mathbf{s}}_{\ell m}^{\text{ref}}. \quad (3.24)$$

In particular, because the reference case differs from the perturbed case only by the absence of the perturbation, this comparison removes the contribution to the residuals from a mismatch between the true foreground SEDs and the model used in the component separation, from the masking procedure and other effects which are present both in the reference and perturbed cases. This justifies the use of simplistic foreground models such as the `d0` and `s0` models from `PySM`.

The bias δr is defined to be the measured value of r assuming its true value to be $r = 0$. Therefore, we can extract it from the power spectrum C_{ℓ}^{res} of the residuals $\delta \mathbf{s}_{\ell m}$ by maximizing the following cosmological likelihood as a function of r :

$$-2 \ln \mathcal{L}_{\text{cosmo}} = f_{\text{sky}} \sum_{\ell} (2\ell + 1) \left(\ln C_{\ell}^{\text{th}}(r) + \frac{C_{\ell}^{\text{th}}(r=0) + C_{\ell}^{\text{res}}}{C_{\ell}^{\text{th}}(r)} \right), \quad (3.25)$$

where C_{ℓ}^{th} is the theoretical CMB B -mode power spectrum that includes all expected contributions:

$$C_{\ell}^{\text{th}} = r C_{\ell}^{\text{GW}} + C_{\ell}^{\text{lens}} + N_{\ell} + R_{\ell}^{\text{fore}}, \quad (3.26)$$

where C_{ℓ}^{GW} is the primordial CMB BB power-spectrum for $r = 1$, C_{ℓ}^{lens} is the contribution from gravitational lensing, N_{ℓ} is the power-spectrum of the noise after component separation and R_{ℓ}^{fore} is the expected power-spectrum of foreground residuals from statistical uncertainties propagated through component separation. The contributions N_{ℓ} and R_{ℓ}^{fore} are estimated following [15].

4 Results

The purpose of this section is to use the frameworks described in Section 3 to build the bridge between scientific requirements for *LiteBIRD* and requirements on the instrument knowledge for the specific case of beam far-sidelobes. Table 2 describe how the results for the various cases and methods are organized in the Section.

	Perturbation Case	Modeling Case
Detailed Method	4.1	
Axisymmetric Method	4.2.1	4.2.2

Table 2: Organization of Section 4 for the various cases. We remind the reader that the Perturbation Case corresponds to the study of measurement uncertainties while the Modeling Case corresponds to the study of modeling errors, and that the Detailed Method adopts a full simulation of the asymmetric beam, focal plane and scanning strategy while the Axisymmetric Method follows an axisymmetric map-based approach.

4.1 Requirements for the Perturbation Case

4.1.1 Bias on the tensor-to-scalar ratio from the beam perturbation

The goal of this section is to use the approach described in 3.1.1 to evaluate the impact of an imperfect beam knowledge from calibration errors and to produce requirements on calibration measurements given the methodology assumptions of this work, detailed in Section 3.

To this aim, we estimate the bias on r introduced by a perturbation of the beam in a single frequency channel and in a single angular window at a time, with a perturbation amplitude $\alpha^{\nu,W}$, following Eq. (3.6) and the corresponding beam Eq. (3.8). The beams in other channels are left unperturbed such that the induced bias on the tensor-to-scalar ratio $\delta r^{\nu,W}$ comes only from the perturbed channel. From a given set of arbitrarily assigned error budgets per channel $\delta r_{\text{lim}}^{\nu,W}$, we find the corresponding limit values $\alpha_{\text{lim}}^{\nu,W}$ of the amplitudes $\alpha^{\nu,W}$ that induce a bias $\delta r^{\nu,W} = \delta r_{\text{lim}}^{\nu,W}$. We found that the bias on r scales as $\delta r \propto \alpha^2$, as can be seen in Figure 7. This is to be expected since α scales the amplitude of the perturbation, therefore the power-spectrum is scaled by α^2 .

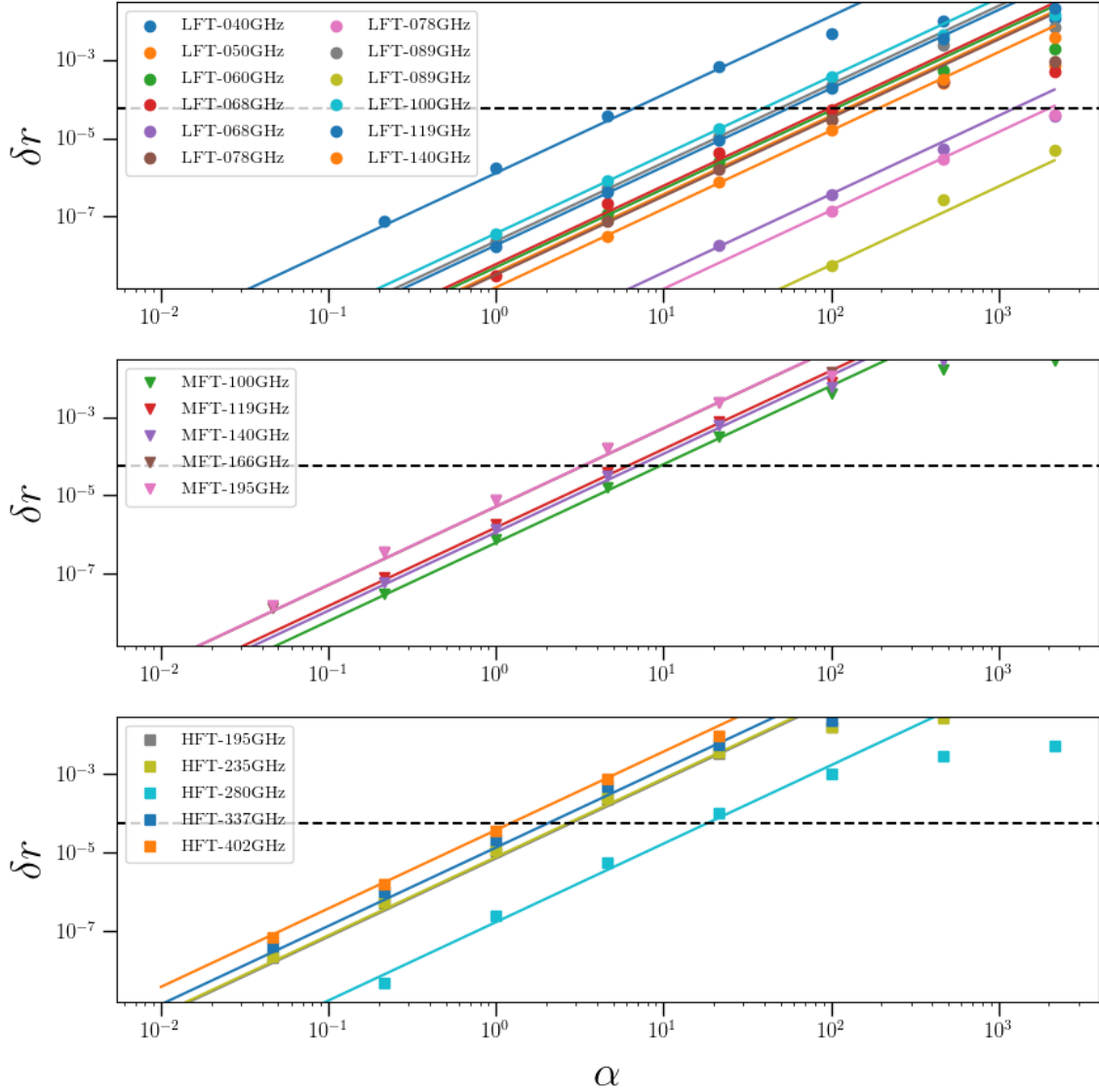


Figure 7: Evolution of the bias on r as a function of α in each frequency channel of the LFT (top), MFT (middle) and HFT (bottom). The solid lines correspond to the quadratic law $\delta r_{\nu} \propto \alpha_{\nu}^2$ that best fits the points at perturbation amplitudes $\alpha \leq 100$, where the quadratic scaling breaks down in frequency channels that induce a large bias. These results are obtained in the angular window at largest angle for illustration, the behaviour in the two other windows being similar.

If we assume the effect on each channel to be independent, which is a reasonable assumption for small biases as is the case in this study, $a_{\ell m}$ of the corresponding residuals would add in quadrature. So, because δr is the amplitude of their variance the total bias is obtained by simply summing the biases from the different channels. Therefore, the total bias will correspond to the total error budget assigned to the beams far side-lobe systematic effect $\Delta r_{\text{FSL}} = \sum_{\nu, W} \delta r_{\text{lim}}^{\nu, W}$. We follow the total budget for beam far side-lobe systematic bias defined by the *LiteBIRD* collaboration: $\Delta r_{\text{FSL}} = 1.9 \times 10^{-5}$ [15]. Note that this corresponds to $\sim 3\%$ of the total mission systematic budget which is $0.001/\sqrt{3}$. We further assume, for now, that each channel have the same contribution to Δr . In our case, there are 22 frequency channels and 3 angular windows, so the allowed bias from each channel is assigned with equal weight and is simply $\delta r_{\text{lim}}^{\nu, W} = (1.9/66) \times 10^{-5}$. Note that assuming different values of Δr_{FSL} or $\delta r_{\text{lim}}^{\nu, W}$ would lead to different requirements.

In order to check that the correlation between the effect in the different frequency channels is limited, we estimated the total contribution Δr with a hundred realizations of simultaneously varying the perturbation amplitudes $\alpha^{\nu, W}$ in all frequency channels at once but treating the angular windows separately, with a uniform distribution in the range $\left[\max\left(-W_{\text{max}}^{-1}, -\sqrt{3}\alpha_{\text{lim}}^{\nu, W}\right); \sqrt{3}\alpha_{\text{lim}}^{\nu, W} \right]$. We use a uniform distribution instead of a Gaussian distribution with standard deviation $\alpha_{\text{lim}}^{\nu, W}$ to avoid negative beam amplitudes. Nevertheless, we maintain the same variance as the Gaussian distribution by introducing a factor of $\sqrt{3}$ to the width of the uniform distribution. The average bias due to the far side-lobe systematic effect is found to be $\Delta r = 2.08 \times 10^{-5}$, in excess by less than $\sim 10\%$ as compared to the pre-defined bias budget defined above which we consider as validating our assumption of small correlations between the channels. Note that these results are slightly different as those presented in [15] where it was assumed that $\alpha \geq -1$, which tends to over-estimate the average bias compared to the more precise limit used here. The average residual power spectra are shown in Figure 8.

From this procedure, we derive requirements on the perturbation amplitudes $\alpha^{\nu, W}$, given $\delta r_{\text{lim}}^{\nu, W}$, as an upper bound $\alpha_{\text{lim}}^{\nu, W}$. However, though the α_{lim} parameters are useful intermediate to evaluate the effect of imperfect beam knowledge, they are not directly accessible and we want to relate them to physical properties of the beams. We describe three such properties in the following sections.

4.1.2 Beam perturbation power

First, we introduce the parameter δR_{lim} that quantifies the relative difference of power between the perturbed and unperturbed beams:

$$\delta R_{\text{lim}}^{\nu, W} \equiv \frac{\int B_{\text{lim}}^{\nu, W}(\theta) W(\theta) d\Omega}{\int \overline{B}_0^{\nu}(\theta) d\Omega}. \quad (4.1)$$

In this expression, we defined the fractional power difference between the perturbed and nominal beams $B_{\text{lim}}^{\nu, W}(\theta) = \alpha_{\text{lim}}^{\nu, W} \overline{B}_0^{\nu}(\theta)$ with the averaged beam normalized at the peak, i.e. $\overline{B}_0^{\nu}(\theta = 0) = 1$ as will always be the case in the following. This quantity clearly represents the fraction of power in the perturbation expressed in units of the total power of the beam, and is illustrated in Figure 9 for the LFT 100 GHz channel. The $\delta R_{\text{lim}}^{\nu, W}$ values found in the 22 frequency channels and three angular windows are given in Table 3.

We can see a remarkable fact from these requirements: they show little dependence on the angular range. In a given frequency channel, the difference between requirements in the three windows is at most of the order of a few dBis, much less than the variation between frequency channels, despite the large difference between the definitions of the windows. This means that the requirements on δR_{lim} are quite independent of the beam shape and of the shape of the perturbation. So, the difference of power between the perturbed and unperturbed beams is the leading effect to the bias on r . And the relative differences in sensitivity between frequency channels come from their weight in the component separation, i.e. from the relative amplitude of Galactic foreground emissions in these channels. In particular, the requirements are the most stringent for the lowest frequency channel, important to clean for synchrotron, around the CMB frequencies and for the high frequency channels, important to clean for dust. Therefore, we believe that improving the beam modeling would not change significantly the requirements on δR_{lim} .

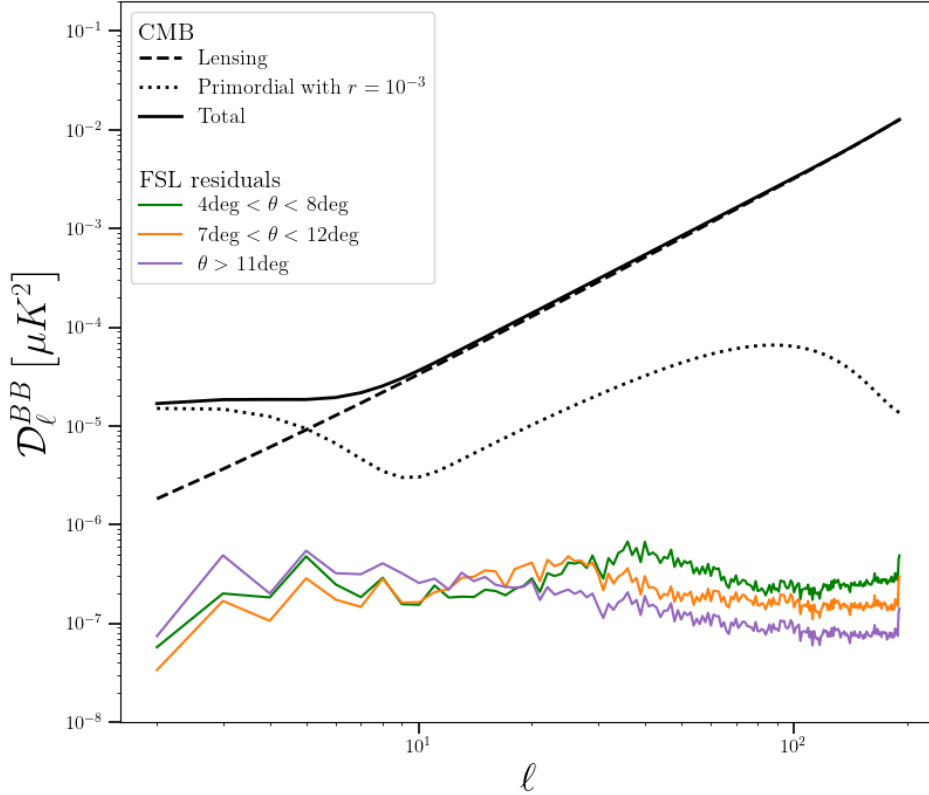


Figure 8: Average of the residual B -mode power spectra from beam far side-lobes mismatch in the 3 angular windows, for 100 realizations of randomly produced sets of perturbation amplitudes $\alpha^{\nu,W}$ parameters following the requirements that $\alpha^{\nu,W} \in \left[\max\left(-W_{\max}^{-1}, -\sqrt{3}\alpha_{\text{lim}}^{\nu,W}\right); \sqrt{3}\alpha_{\text{lim}}^{\nu,W} \right]$ for all frequency channels in the given angular window. The corresponding total bias on r is evaluated, combining the three windows and using (3.25), to be $\Delta r = 2.08 \times 10^{-5}$.

However, δR_{lim} is not directly measurable because the total beam power, i.e. the integral of the beam appearing in the denominator of Eq. (4.1), is not precisely known. So, despite the apparent robustness of this physical quantity, we have to express requirements in terms of other related quantities.

4.1.3 Average perturbation amplitude in the window

Following the results of the previous subsection, we define δB_{lim} which is closer to what can actually be used as a benchmark for calibration measurements (see also Eq. (4.5)):

$$\delta B_{\text{lim}}^{\nu,W} \equiv \frac{\int B_{\text{lim}}^{\nu,W}(\theta) W(\theta) d\Omega}{\int W(\theta) d\Omega} = \frac{\int \overline{B_0^\nu}(\theta) d\Omega}{\int W(\theta) d\Omega} \delta R_{\text{lim}}^{\nu,W}. \quad (4.2)$$

This quantity corresponds to the average amplitude, normalized to the peak, of the perturbation in the angular window and is illustrated in Figure 9. It is clear on one hand that δB_{lim} is easier to measure than δR_{lim} but on the other hand that the requirements will depend on the definition of the windows. In particular, the larger the window the more stringent the requirements on δB_{lim} . This is

δR_{lim} (dBi)											
ν (GHz)	LFT										
	40	50	60	68	78	89	100	119			
$4^\circ < \theta < 8^\circ$	-23.54	-13.45	-17.68	-13.27	-8.02	-18.36	-16.43	-23.14	-15.50	-25.61	-27.57
$7^\circ < \theta < 12^\circ$	-25.41	-15.51	-19.68	-15.75	-10.99	-19.21	-17.28	-24.13	-16.49	-26.59	-28.46
$11^\circ < \theta$	-27.49	-17.44	-21.53	-18.20	-13.67	-17.41	-16.18	-23.40	-16.27	-26.01	-27.86

ν (GHz)	LFT	MFT					HFT				
	140	100	119	140	166	195	195	235	280	337	402
$4^\circ < \theta < 8^\circ$	-23.23	-26.84	-29.71	-23.92	-34.64	-37.07	-33.00	-35.65	-32.52	-41.78	-38.03
$7^\circ < \theta < 12^\circ$	-23.88	-27.90	-30.71	-24.61	-35.63	-37.89	-34.17	-36.60	-33.34	-42.66	-38.68
$11^\circ < \theta$	-26.69	-25.74	-29.20	-29.83	-33.91	-34.30	-32.73	-34.38	-27.26	-37.79	-38.93

Table 3: Beam perturbation requirements for each frequency channel and each of the three angular windows of the beam perturbations giving $\delta r = 1.9 \times 10^{-5}/66$, using unperturbed beams in the other frequency channels and angular windows. These results are expressed in terms of δR_{lim} , in dBi. The color of the cells correspond to a linear scale from green for the easiest requirements (on δR_{lim}) to red for the most challenging.

particularly relevant for the last angular window, which in principle ranges from $\sim 11^\circ$ up to $\sim 180^\circ$, combining regions with very different power levels. This would lead to unreasonably low requirements for δB_{lim} in the last angular window. So, we have to make a choice of upper bound up θ_{max} to which we should compute the integrals in the definition Eq. (4.2), based on beam dependent considerations. This makes the requirements on δB_{lim} dependent on the beam modeling.

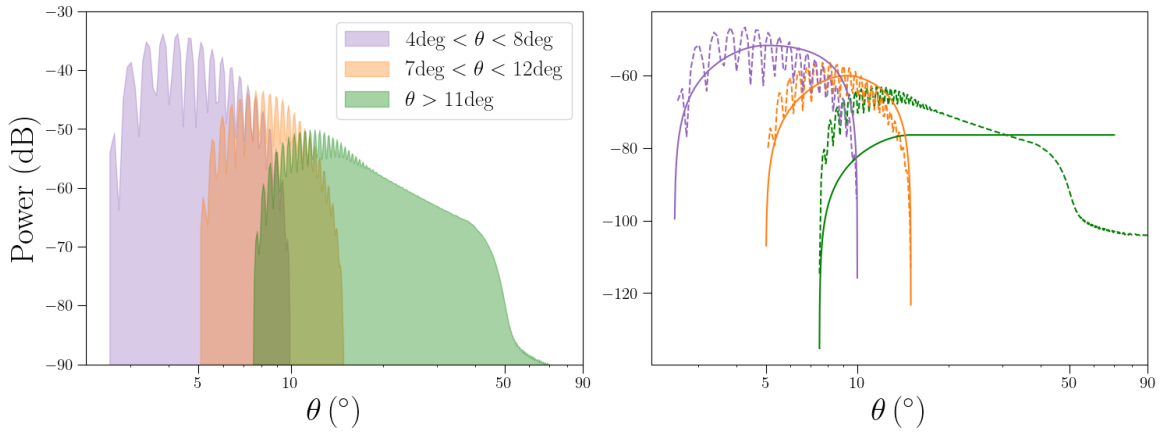


Figure 9: (Left) Illustration of δR_{lim} as the shaded area in the three angular windows in *LiteBIRD*'s 100 GHz LFT channel, for a perturbation amplitude $\alpha = 1$. (Right) Illustration of δB_{lim} in the same channel for $\alpha = 1$. The dashed lines correspond to the actual beam perturbations, while the solid lines represent what would be the perturbations if $\overline{B_0^2}(\theta)$ was constant in the window, equal to δB_{lim} .

Because the amplitude of the beam models used for this analysis drops drastically at angles larger than $\sim 50^\circ$ (and are expected to decrease significantly at large angle thanks to the design of *LiteBIRD*), this upper bound should not be too much higher than $\sim 50^\circ$. To stay conservative, we show the requirements on δB_{lim} in Table 4 where we restrict the last window to angles smaller than 70° .

δB_{lim} (dB)											
ν (GHz)	LFT										
	40	50	60	68		78		89		100	119
$4^\circ < \theta < 8^\circ$	-42.55	-34.09	-39.46	-36.70	-30.45	-42.82	-39.42	-48.56	-38.84	-51.80	-54.82
$7^\circ < \theta < 12^\circ$	-46.62	-38.35	-43.67	-41.38	-35.62	-45.87	-42.48	-51.75	-42.04	-54.98	-57.91
$11^\circ < \theta < 70^\circ$	-66.40	-57.98	-63.20	-61.52	-56.00	-61.76	-59.07	-68.70	-59.51	-72.09	-75.00
ν (GHz)	LFT	MFT					HFT				
	140	100	119	140	166	195	195	235	280	337	402
$4^\circ < \theta < 8^\circ$	-51.25	-50.65	-54.58	-49.55	-60.87	-63.56	-59.01	-62.92	-60.57	-70.48	-67.91
$7^\circ < \theta < 12^\circ$	-54.11	-53.91	-57.78	-52.45	-64.07	-66.58	-62.38	-66.07	-63.60	-73.57	-70.77
$11^\circ < \theta < 70^\circ$	-74.60	-69.44	-73.96	-75.36	-80.06	-80.69	-78.63	-81.55	-75.23	-86.41	-88.72

Table 4: Beam perturbation requirements for each frequency channel and each of the three angular windows of the beam perturbations giving $\delta r = 1.9 \times 10^{-5}/66$, using unperturbed beams in the other frequency channels and angular windows. These results are expressed in terms of δB_{lim} , in dB, assuming the last angular window to range up to 70° . The color of the cells correspond to a linear scale from green for the easiest requirements (on δB_{lim}) to red for the most challenging.

As expected, the most challenging window and frequency channels are the one at large angle covering the largest area and at high frequencies. This comes from two effects: the importance of high frequency channels to estimate with a good lever arm the dust signal in channels at CMB frequencies, and the small FWHM of high frequency channels leading to very low average amplitude at large angles. In this context, it is clear that assigning the same bias budget to all channels is not optimal in terms of requirements, and we can alleviate a little the requirements in the most sensitive channels by making those in the other channels more stringent.

Having this in mind, we derived the requirements on δB_{lim} assuming the whole frequency and angular range to share the same calibration accuracy. In this case, the requirement will be expressed as a single common $\overline{\delta B_{\text{lim}}}$, that we obtain by tuning the single channel bias budget $\delta r_{\text{lim}}^{\nu,W}$ such that $\delta B_{\text{lim}}^{\nu,W} = \overline{\delta B_{\text{lim}}}$. It is possible to compute analytically an estimation of $\overline{\delta B_{\text{lim}}}$ using the previously found values of $\alpha_{\text{lim}}^{\nu,W}$ parameters with the scaling $\delta r^{\nu,W} \propto (\alpha^{\nu,W})^2$. This leads to the following expression:

$$\overline{\delta B_{\text{lim}}} = \sqrt{\frac{n_\nu \times n_\theta}{\sum_{\nu,W} (\delta B_{\text{lim}}^{\nu,W})^{-2}}}, \quad (4.3)$$

where n_θ is the number of angular windows, $\delta B_{\text{lim}}^{\nu,\theta}$ are the requirements previously found. In the case where δB_{lim} is defined up to 70° , these are taken from Table 4, and we find the common precision requirement to be $\overline{\delta B_{\text{lim}}} = -80.42$ dB. In other words, under our assumptions the beam amplitude must be known in each frequency channel and each window with a precision of $\sim 10^{-8}$ with respect to the peak, including systematic and statistical sources of errors during calibration. Once again, this result depends on the definition of the windows, and in particular on the maximum angle θ_{max} of the last window. If θ_{max} is different, to reflect more accurately our knowledge of the optical characteristics of the telescope, or to investigate the potential impact of other design choices, this would have a significant impact on the value of $\overline{\delta B_{\text{lim}}}$. The left part of Figure 10 shows how $\overline{\delta B_{\text{lim}}}$ varies as a function of θ_{max} , keeping δR_{lim} constant as we saw that it should not depend on the window.

To put these requirements into perspective, one can compare with the level of accuracies that were reached for Planck during the ground calibration campaign. The difference between modeling

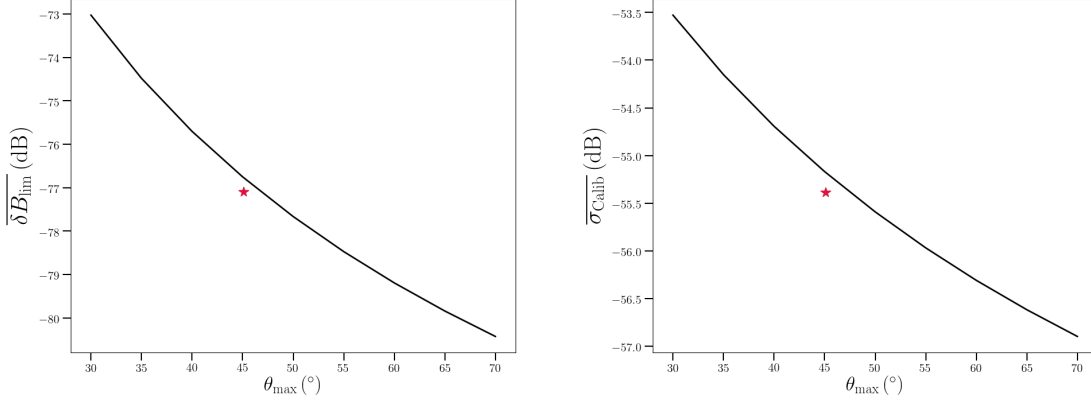


Figure 10: (Left) Evolution of the common requirement $\overline{\delta B_{\text{lim}}}$ defined in Eq. (4.3) as a function of the upper bound angle θ_{max} after which the last angular window is $W(\theta > \theta_{\text{max}}) = 0$. In the definition of δB_{lim} Eq. (4.2), δR_{lim} is kept constant as it is rather stable with respect to the definition of the windows. The red star corresponds to the value of $\overline{\delta B_{\text{lim}}}$ when $\theta_{\text{max}}^{\nu}$ is obtained in each channel such that $\int_{\theta_{\text{max}}^{\nu}} \overline{B_0^{\nu}}(\theta) W(\theta) d\Omega$ include 97.5% of the theoretical perturbation power, at the mean of the $\theta_{\text{max}}^{\nu}$. (Right) Evolution of the common requirement $\overline{\sigma_{\text{Calib}}}$ defined in Eq. (4.5) as a function of θ_{max} under the same assumptions.

and measurements was of the order of 6 dB for iso-levels of -90 dB at 100 GHz, and 7 dB at -80 dB at 320 GHz [40].

4.1.4 Noise limited calibration measurements

If calibration measurements of the beams face systematic sources of errors, the requirements that apply to the accuracy of calibration measurements are the ones set for δB_{lim} in the previous subsection. However, in the case of noise limited measurements, we do not need to go to such accuracy, because we can make several independent measurements of the same perturbation in many pixels on the sphere, distributed in the 2D angular ring of the perturbation. To make this more precise, the quantity effectively measured during ground beam calibration is the integrated power measured in a certain region of the sphere, normalized to the integrated power measured at the beam center, which can be modeled as:

$$P_{\text{Calib}}^{\nu}(\hat{r}) \equiv \int \overline{B_0^{\nu}}(\theta) \omega(\hat{r}' - \hat{r}) d\Omega' \frac{1}{\int \overline{B_0^{\nu}}(\theta) \omega(\hat{r}') d\Omega'} + n_{\text{Calib}}, \quad (4.4)$$

where $\omega(\hat{r})$ is a small integration window of the beam that can be interpreted as a pixel in the (θ, ϕ) surface and n_{Calib} the noise in the beam calibration measurements.

We estimate the precision required on the measured quantity $P_{\text{Calib}}(\hat{r})$ assuming random uncorrelated errors in each measurement (and hence no systematic effects), and a grid of measurements at many angles as illustrated in Figure 11. In this case the calibration measurement uncertainty $\sigma_{\text{Calib}} = \sqrt{\langle n_{\text{Calib}} n_{\text{Calib}}^T \rangle}$ is related to the quantity δB_{lim} by:

$$\sigma_{\text{Calib}}^{\nu, W} = \frac{\int W(\theta) d\Omega}{\sqrt{\sum_{ij} W^2(\theta_{ij}) \Delta\Omega_{\text{pix}}}} \delta B_{\text{lim}}^{\nu, W} \equiv \sqrt{N_{\text{eff}}^W} \delta B_{\text{lim}}^{\nu, W}, \quad (4.5)$$

with $\Delta\Omega_{\text{pix}}$ the solid angle covered by one calibration measurement and i, j the pixel number for a pixelized beam calibration map. The quantity σ_{Calib} can directly be interpreted as the accuracy of the beam measurements. In all of the following, we assume arbitrarily a constant pixel size $\Delta\Omega_{\text{pix}} =$

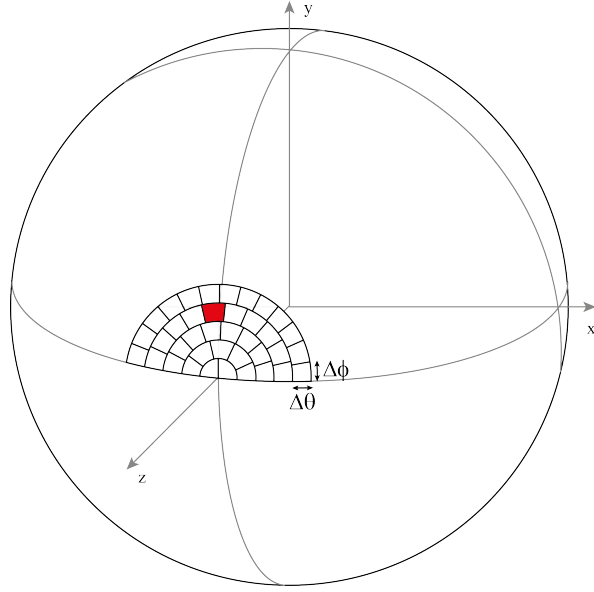


Figure 11: Illustration of the grid of beam measurement pixels on the sphere. Each pixel, as the highlighted red one, is supposed to have the same area and are distributed in rings of constant $\Delta\theta$.

$0.5^\circ \times 0.5^\circ = 0.25 \text{ deg}^2$, during beam ground calibration, but different values of Ω_{pix} would lead to different requirements on σ_{Calib} . As already mentioned, we assume the calibration beam measurements to be normalized to one at the peak. The factor N_{eff}^W is the effective number of pixels in the region of the beam perturbation. As in the case of δB_{lim} , the requirements will depend on the definition of the windows. However, the dependency on the windows is not as straightforward because, as θ_{max} in the last window is reduced, for instance, the effective number of pixel will decrease while δB_{lim} will increase. The requirements for σ_{Calib} assuming $\theta_{\text{max}} = 70^\circ$ are given in Table 5, where the effective numbers of pixels are $N_{\text{eff}} = 742.0, 1541.9, \text{ and } 52943.2$ in the three windows from small to large angles respectively.

In the same way as we derive a common requirement $\overline{\delta B_{\text{lim}}}$ using Eq. 4.3, we can also derive a single common $\overline{\sigma_{\text{Calib}}}$. Under our general assumptions and assuming $\theta_{\text{max}} = 70^\circ$, we find $\sigma_{\text{Calib}} = -56.90 \text{ dB}$, and the θ_{max} dependence of σ_{Calib} is shown in the right panel of Figure 10.

4.2 Requirements for the Modeling Case

4.2.1 Comparison of the Detailed Method and the Axisymmetric Method

The Axisymmetric Method, based on the axisymmetric beam approximation we detailed in Section 3.1.2, needs to be validated before being used for the purpose of investigating modeling uncertainties. This is done by comparing the results described in the previous section obtained using the Detailed Method with results obtained under the axisymmetric approximation. We use the pipeline of the Perturbation Case described in Section 3.1.1, but here the input 4π maps and side-lobes maps are calculated with the averaged and symmetrized GRASP beams following the description of Section 3.1.2. The corresponding perturbed maps are then produced using Eq. 3.5. To perform a meaningful comparison, we perturb the beam in the same three angular windows and keep the same bias budget in each channel $\delta r_{\text{lim}}^{\nu, W} = (1.9/66) \times 10^{-5}$. The results of the comparison between the two methods are given in Table 6, expressed as $\delta B_{\text{lim}}^1 - \delta B_{\text{lim}}^2$ where δB_{lim}^i is obtained using Method i . The values of δB_{lim}^2 in each frequency channel show a good agreement, with a difference with δB_{lim}^1 of a few dBs, up to a little more than $\sim 3 \text{ dB}$ in a few channels. We also note that the Axisymmetric Method seems to systematically underestimate the bias on r which leads to a systematically higher δB_{lim} . Although the origin of such a factor of 2 of difference in some channels needs to be further understood, given

σ_{Calib} (dB)											
ν (GHz)	LFT										
	40	50	60	68		78		89		100	119
$4^\circ < \theta < 8^\circ$	-28.20	-19.73	-25.11	-22.34	-16.10	-28.46	-25.07	-34.20	-24.49	-37.45	-40.47
$7^\circ < \theta < 12^\circ$	-30.68	-22.41	-27.73	-25.44	-19.68	-29.93	-26.53	-35.81	-26.10	-39.04	-41.97
$11^\circ < \theta < 70^\circ$	-42.79	-34.37	-39.60	-37.92	-32.39	-38.16	-35.46	-45.10	-35.91	-48.49	-51.39
ν (GHz)	LFT	MFT					HFT				
	140	100	119	140	166	195	195	235	280	337	402
$4^\circ < \theta < 8^\circ$	-36.90	-36.30	-40.23	-35.20	-46.52	-49.20	-44.65	-48.57	-46.22	-56.12	-53.56
$7^\circ < \theta < 12^\circ$	-38.17	-37.97	-41.84	-36.51	-48.13	-50.64	-46.44	-50.13	-47.66	-57.63	-54.83
$11^\circ < \theta < 70^\circ$	-51.00	-45.84	-50.36	-51.76	-56.45	-57.08	-55.03	-57.95	-51.63	-62.81	-65.12

Table 5: Beam perturbation requirements for each frequency channel and each of the three angular windows of the beam perturbations giving $\delta r = 1.9 \times 10^{-5}/66$, using unperturbed beams in the other frequency channels and angular windows. These results are expressed in terms of σ_{Calib} , in dB, assuming the last angular window to range up to 70° and a constant pixel size $\Delta\Omega_{\text{pix}} = 0.5^\circ \times 0.5^\circ$. The color of the cells correspond to a linear scale from green for the easiest requirements (on σ_{Calib}) to red for the most challenging.

that the results span almost six orders of magnitude (60 dB) throughout the different windows and frequency channels, this is still an impressive agreement. This implies that the asymmetries of the beam do not have a significant impact on our analysis, possibly thanks to the scanning strategy of *LiteBIRD* which is efficient in symmetrizing the given GRASP beam. Note that the *LiteBIRD* GRASP beams in this study do not have significant asymmetric features as explained in Section 3.1.1. The case of more realistic beam asymmetries will be studied in a future work.

δB_{lim}^1 (dB) – δB_{lim}^2 (dB)											
ν (GHz)	LFT										
	40	50	60	68		78		89		100	119
$4^\circ < \theta < 8^\circ$	-1.63	-1.88	-1.56	-1.45	-0.31	-1.62	-1.60	-1.93	-1.79	-2.19	-2.59
$7^\circ < \theta < 12^\circ$	-1.91	-1.48	-1.63	-1.59	-0.96	-2.24	-2.18	-2.46	-2.29	-2.63	-2.99
$11^\circ < \theta < 70^\circ$	-1.45	-1.15	-1.24	-1.09	-0.89	-1.54	-1.58	-1.90	-1.80	-2.14	-2.44
ν (GHz)	LFT	MFT					HFT				
	140	100	119	140	166	195	195	235	280	337	402
$4^\circ < \theta < 8^\circ$	-3.91	-1.76	-2.23	-3.63	-1.64	-1.92	-1.19	-1.67	-2.66	-2.82	-3.11
$7^\circ < \theta < 12^\circ$	-3.68	-2.26	-2.73	-3.13	-1.88	-1.99	-1.86	-2.06	-3.03	-3.08	-3.28
$11^\circ < \theta < 70^\circ$	-2.33	-1.94	-2.22	-2.18	-2.08	-2.08	-1.82	-1.76	-2.46	-2.97	-3.46

Table 6: Difference in dB between δB_{lim} obtained from measurement uncertainties approach (Section 3.1.1) and the corresponding δB_{lim}^2 obtained using the axisymmetric approach (Section 3.1.2) for each frequency channel and each of the three angle ranges of the beam perturbations giving $\delta r_{\text{lim}}^{\nu, W} = 1.9 \times 10^{-5}/66$.

In consideration of flexibility and less time consumption, we apply the new approach in the following study of modeling uncertainties.

4.2.2 Bias on the tensor-to-scalar ratio from beam mismodeling at large angle

The main goal of this section is to find a way of figuring out the limit angle θ_{lim} after which we can rely entirely on modeling to correct for beam effects. This angle will depend strongly on the ability of the beam model to reproduce key features of the true beam. Therefore, we have to explore the impact of both parameters of the beam model Eq. (3.11), θ_{lim} and b , at the same time. Following the same idea as in section 4.1, Figure 12 shows the bias on r on a grid of (θ_{lim}, b) values when perturbing a single channel at a time keeping the other channels unperturbed, in three selected frequency channels: at the lowest frequency 40 GHz of the LFT, in one of the CMB frequency channels at 140GHz of the MFT and at the highest frequency 402 GHz of the HFT which we know from the previous section give the tightest constraints. In these figures, the region on the left of the black contour corresponds to sets of parameters for which $\delta r^\nu > \delta r_{\text{lim}}^\nu$, the allocated budget in the given frequency channel, and the region on the right is where $\delta r^\nu < \delta r_{\text{lim}}^\nu$. Following the spirit of the previous section when dealing with calibration uncertainties, we allocate the same budget to every frequency channel, namely $\delta r_{\text{lim}}^\nu = \Delta r_{\text{FSL}}/n_\nu = 1.9 \times 10^{-5}/22$.

As we can see in each of these figures, neither of the flat beam model ($b = 0$) and the cut beam model ($b \rightarrow \infty$), allow to reach θ_{lim} close to the lowest possible values. In each frequency channel, there is a value of b for which the limit bias is achieved for a lower value of θ_{lim} . This corresponds to the value of b for which the power law beam model best fits the reference beam, leading to an induced bias compatible with the budget for lower values of θ_{lim} . However, the power law model is very simple and can only reproduce the most basic of properties from the reference beam. In other words, at least after some angle, the measurement of r is not sensitive to the particular shape of the beam but to other features of the beam that are necessary global in nature such that they can be reproduced by a simple power law model.

Capitalizing on our results of the previous section, we investigate the link between δr^ν and the residual beam power between the true beam and the model:

$$\delta K_{\text{lim}}^\nu(\theta_{\text{lim}}, b) = \left| \int_0^{2\pi} \int_{\theta_{\text{lim}}}^{180^\circ} [B_{\text{model}}^\nu(\theta; \theta_{\text{lim}}, b) - \overline{B_0}^\nu(\theta)] \sin\theta d\theta d\phi \right|. \quad (4.6)$$

The meaning of the δK_{lim} parameter is illustrated in Figure 13 in the LFT 100 GHz channel and for $b = 6$. If the beam profile is normalized by the integral of the beam power, this quantity is equivalent to the δR_{lim} parameter in the previous section that we saw seemed to be a robust quantity across the angular range. We keep a different name for this quantity to emphasize the fact that δR_{lim} is defined for a perturbation around a central beam with the same shape, while δK_{lim} corresponds to a mismatch between a model and the true beam. To verify that δK_{lim} is indeed a relevant parameter, we computed its value on the same grid of (θ_{lim}, b) as before and compared it to the corresponding values of δr . This is illustrated in Figure 14. The two parameters seem to have a similar behaviour in the 2D parameter plane. This is even more striking when looking at what happens for fixed values of θ_{lim} , i.e. for vertical slices. Indeed, in this context, we see that the value of b that corresponds to the minimum of δr is very close to the minimum of δK_{lim} . Up to a very good accuracy, it appears that the power law that induces the least bias is the one that minimizes the residual power after θ_{lim} , regardless of the actual beam shape. For comparison, we also show the minimum of another quantity, $\delta K_{\text{lim}}^{(2)}$, which corresponds to a χ^2 between the reference beam and the beam model, defined as follow:

$$\delta K_{\text{lim}}^{(2)}(\nu, \theta_{\text{lim}}, b) = \int_0^{2\pi} \int_{\theta_{\text{lim}}}^{180^\circ} [B_{\text{model}}^\nu(\theta; \theta_{\text{lim}}, b) - \overline{B_0}^\nu(\theta)]^2 \sin\theta d\theta d\phi. \quad (4.7)$$

Although it would be an intuitive parameter to characterize how close the beam model is to the reference model as its minimum is the least square estimation, it is slightly off especially at high frequency. This gives further confidence in the particular relevance of the δK_{lim} parameter, and of the relative lack of importance of the shape of the beam profile.

Figure 15 shows scatter plots in the $(\delta r, (\delta K_{\text{lim}})^2)$ plane with the same grid points used to produce previous plots. We see that the two parameters are tightly correlated. In fact, the bias is

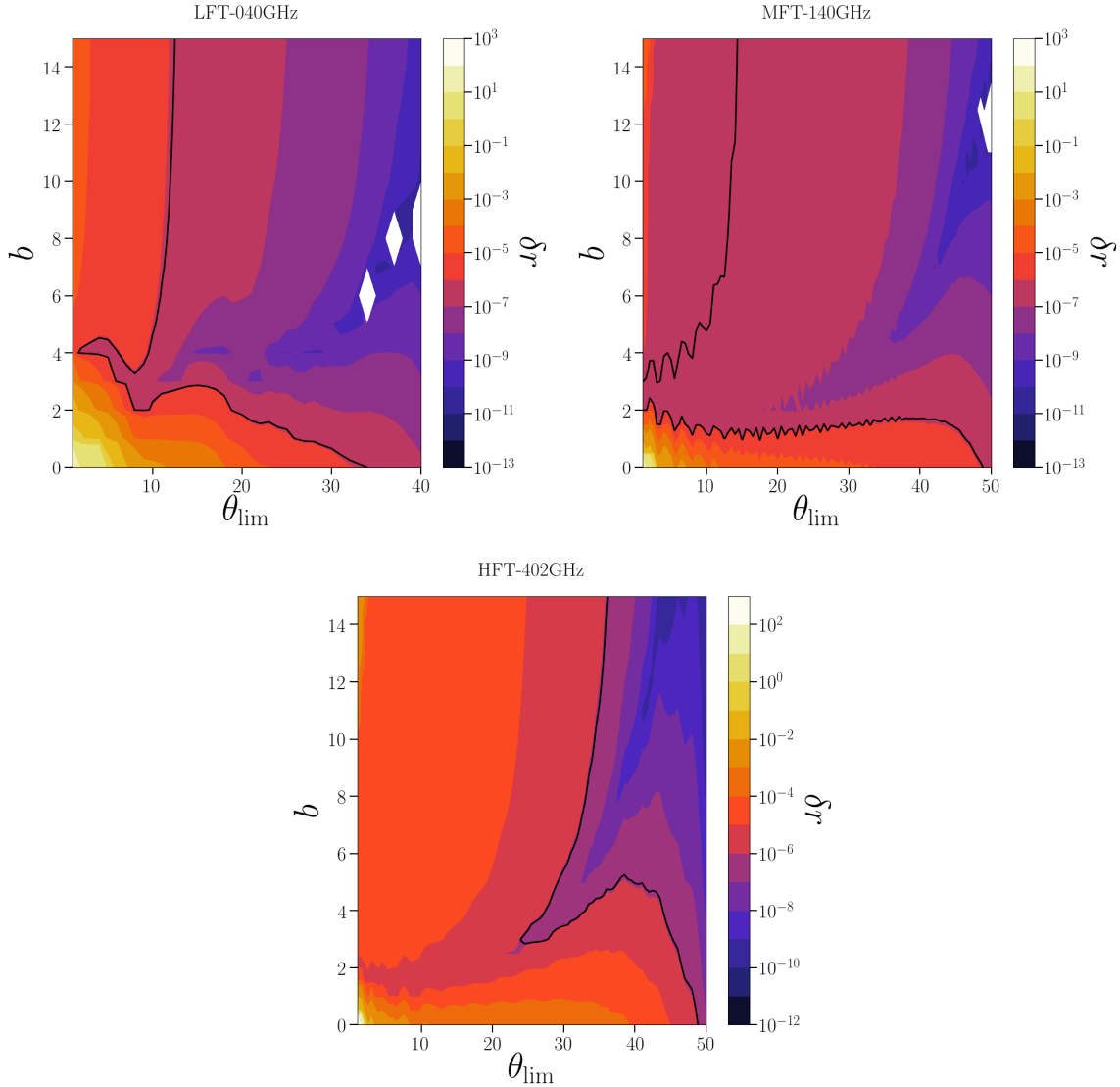


Figure 12: Bias on r in the 2D parameter space (θ_{lim}, b) for three frequency channels, 40 GHz of the LFT (top left), 140 GHz of the MFT (top right) and 402 GHz of the HFT (bottom). The black contours correspond to the limit case where the bias is equal to the systematic error budget allocated to the individual frequency channels, $\delta r = \delta r_{\text{lim}}'' = 1.9 \times 10^{-5} / 22$.

proportional to the residuals power spectrum, i.e. to the correlation of harmonic coefficients, so is proportional to the square of the perturbation at the map level. Therefore, $\delta r \propto (\delta K_{\text{lim}})^2$ as was already pointed out in Section 4.1. The very high correlation between the two parameters means that, to a given requirement on δr would correspond a constant δK_{lim} for all values of θ_{lim} . To further check the correspondence between these two parameters and also to see when it breaks down, we computed the value of δK_{lim} (in units of the total beam integral) for which $\delta r = \delta r_{\text{lim}}$. To compute it, we find the value of b for which $\delta r = \delta r_{\text{lim}}$, for a fixed value of θ_{lim} and assuming that $\int_{\theta_{\text{lim}}}^{180^\circ} [B_{\text{model}}^\nu(\theta; \theta_{\text{lim}}, b) - \overline{B}_0^\nu(\theta)] d\Omega > 0$ to avoid issues coming from the lower bound of this integral corresponding to the case when $b \rightarrow \infty$. The results are shown in Figure 16 in the same three frequency channels as before. We see that, in each channel, there is a θ_{lim} after which we reach a

LFT-100GHz

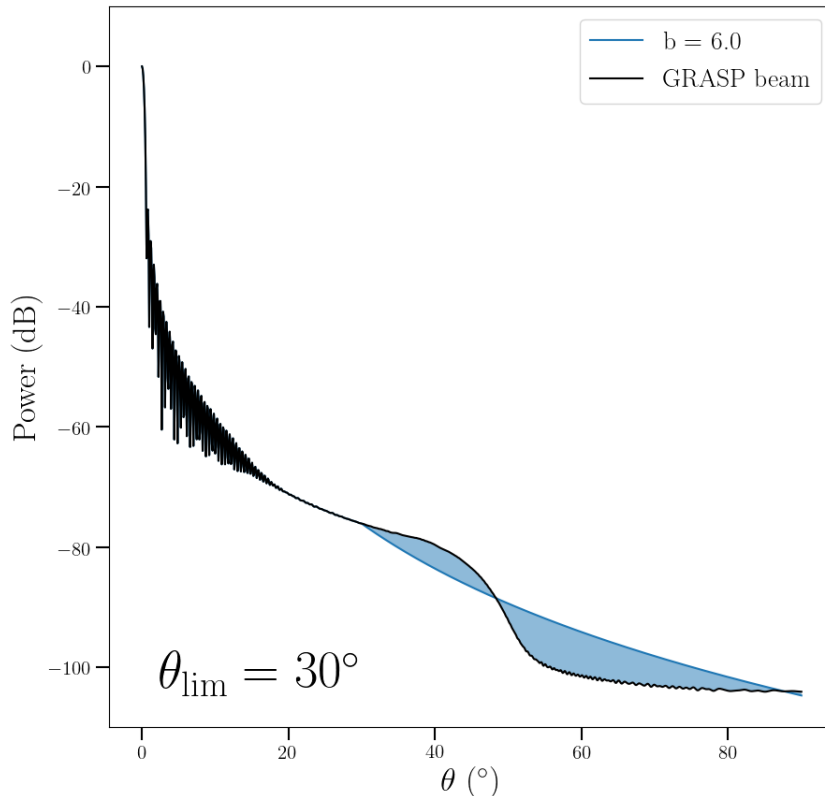


Figure 13: Illustration of the residual power in the θ direction between the true beam and the beam model $\delta K_{\text{lim}}(\theta_{\text{lim}} = 30^\circ, b = 6)$ in the LFT 100 GHz frequency channel as the blue shaded area. The total residual power has to be integrated over ϕ , which in the current context amounts only to a factor of 2π .

regime where δK_{lim} is approximately constant, as expected. For lower values of θ_{lim} , a simple power law is not enough anymore as the actual shape of the beam becomes more important.

Therefore, as we conjectured in the previous section, there is a direct link between the bias on r from the far side-lobes and the relative power difference between the true beam that convolves the sky maps and the beam model used to correct it. This relation can be used to derive meaningful requirements on the needed precision of the modeling: if we have an estimation of the residual power in the far side-lobes region at $\theta > \theta_{\text{lim}}$, δK_{lim} can be interpreted as the required accuracy of this estimation. Alternatively, this relation opens new possibilities to mitigate the effect of the beam far side-lobes by calibrating for δK_{lim} . It can also be used to determine the value of the angle θ_{lim} after which we can rely on the beam model, as the angle at which the relation between δr and δK_{lim} breaks down. In the case of the 3 frequency channels we explored in this section, these angles would be $\sim 10^\circ$ for LFT 40 GHz, $\sim 10^\circ$ for MFT 140 GHz and $\sim 30^\circ$ for HFT 402 GHz.

5 Discussions

Characterizing the beam properties has always been important for CMB space experiments to properly measure CMB intensity and E modes of polarization. The knowledge of the instrument's beam

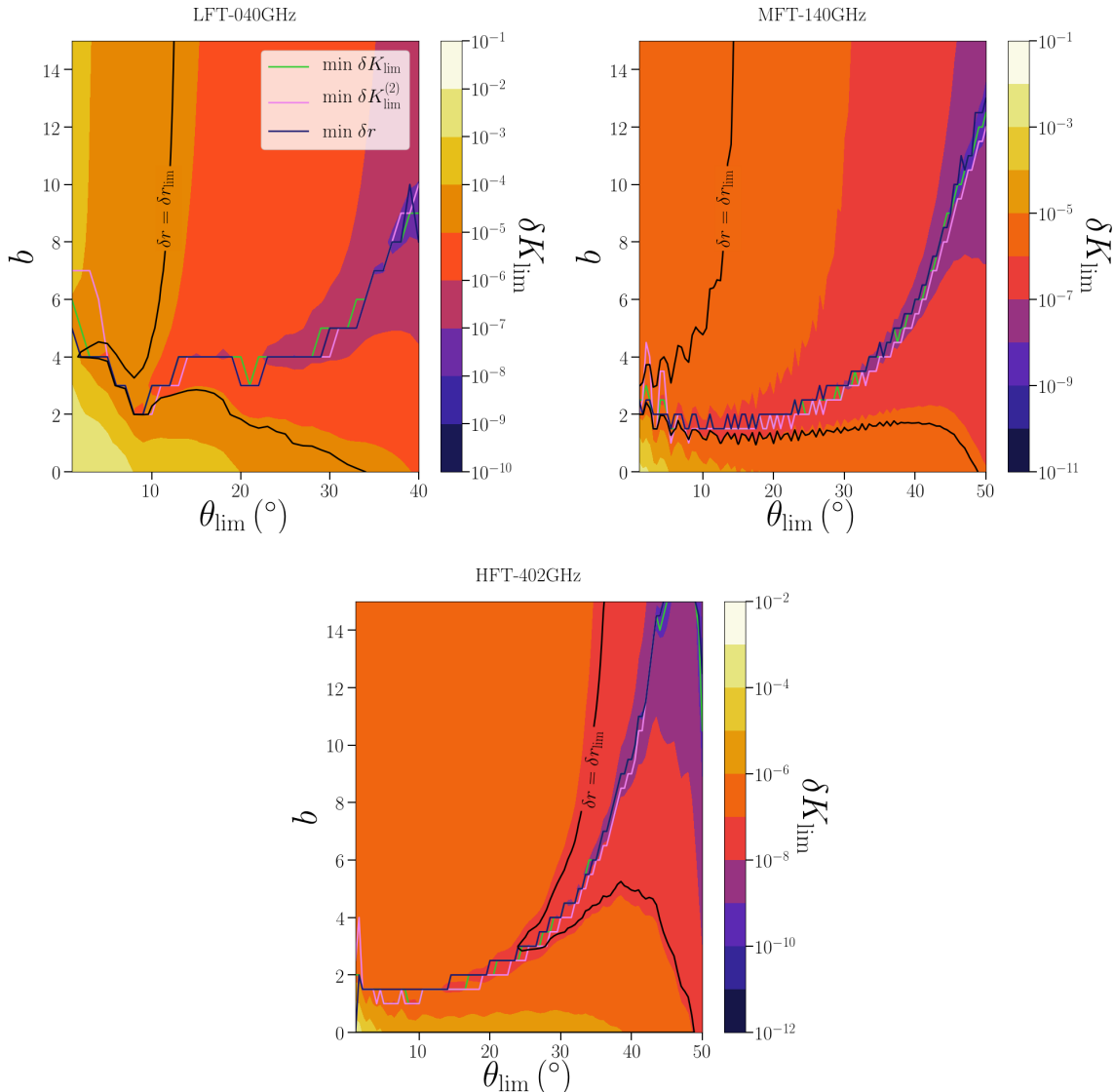


Figure 14: Residual beam power δK_{lim} in the 2D parameter space for three frequency channels, 40 GHz of the LFT (top left), 140 GHz of the MFT (top right) and 402 GHz of the HFT (bottom). The black contours are the same as the ones in Figure 12. The solid blue, green and pink lines correspond to the minimum value of δr , δK_{lim} and $\delta K_{\text{lim}}^{(2)}$ respectively for a given value of θ_{lim} .

characteristics is especially crucial to reach the exquisite level of sensitivity required to detect large-scale CMB B modes. In particular, the beam far side-lobes uncertainty is expected to be one of the main sources of systematic error for *LiteBIRD* [15]. As previously stated, this study is the first to propagate beam systematic effects all the way from their accurate simulation to their impact on cosmological results. We first discuss the requirements for both cases under the assumptions we made in this paper. Then, we further address the limitations and assumptions of this study that leave room to define more meaningful and reliable requirements in future studies. Finally, we describe how the framework developed in this paper could be used to study realistic physical effects with the example of Ruze’s lobes, or to define smooth systematic error curves that are easier to exploit for calibration measurements.

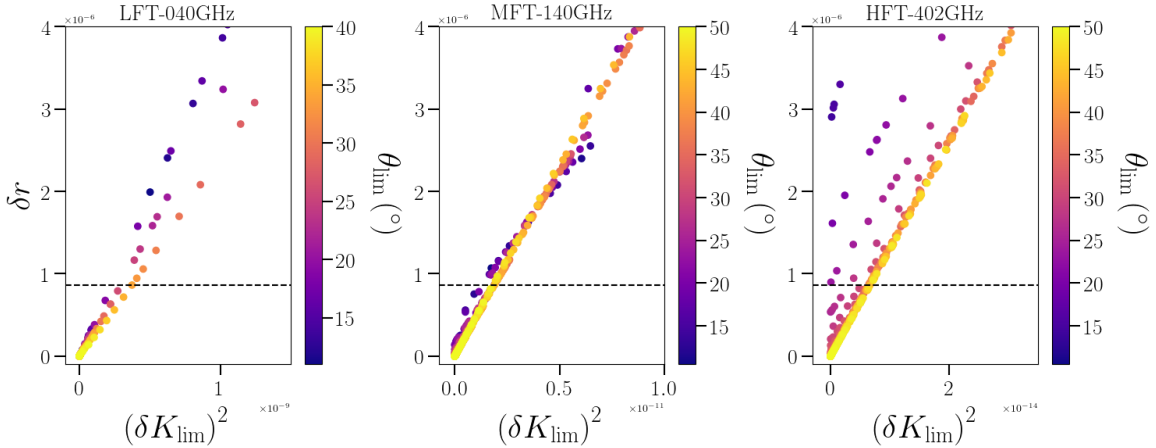


Figure 15: Scatter plot in the 2D $(\delta r, (\delta K_{\text{lim}})^2)$ plane in the grid of θ_{lim} and b values used to produce figures 12 and 14, in the same three frequency channels. Because at very low θ_{lim} , the impact of imperfect beam knowledge is important and cannot be completely grasped by δK_{lim} , we only show the points for which $\theta_{\text{lim}} > 10^\circ$. In addition, the integral in the definition of δK_{lim} is bounded from below by the negative of the reference beam’s integral so only the points where this integral is positive are plotted to facilitate the interpretation. We checked that the high level of correlation between the two parameters still hold when this integral is negative.

5.1 Requirements on calibration

First of all, the comparison between the Detailed Method and the Axisymmetric Method which showed that the results are similar is very important for future studies that will be able to capitalize on the simplicity and flexibility of the axisymmetric approach. In particular, in the following we use this method to understand and interpret the results we obtained.

As explained above, we tried to understand to what extent these results are independent of the particular beams used to convolve the simulated sky maps. Because we are always comparing the perturbed cases with the reference case of convolution with the full unperturbed beam, the analysis itself is only sensitive to the shape of the beam perturbations. In other words, if the perturbation vanishes, so does the bias on r , whatever the beam profile is. In principle in our case, this introduces a dependence on the beam shape because the perturbation is taken to have the same shape as the beam in the angular window of perturbation. In order to quantify how dependent our results are in the beam shape, we followed the Axisymmetric Method using perturbations with a different shape. In analogy with the perturbed beam defined in Eq. (3.8), we used perturbations of the form

$$B_{\text{pert}}^\nu(\theta) = \mu_\nu (B_0^\nu(\theta) + W(\theta) \delta B), \quad (5.1)$$

where δB is a constant parameter that drives the amplitude of the perturbation. The results of the comparison between the constant perturbation Eq. (5.1) and the perturbation defined in Eq. (3.8) are detailed in Table 7, expressed in terms of $\delta B_{\text{lim}} - \delta B_{\text{lim}}^{\text{const}}$ where δB_{lim} is given in Table 4 and $\delta B_{\text{lim}}^{\text{const}}$ is obtained using Eq. (5.1). These results must be compared with results of Table 6. We see that the results are very similar, which supports the claim that our results depend little on the shape of the beam perturbation.

Since the results depend on the perturbation windows, their choice is important and needs to be motivated. The choice of the three windows we made here (see Figure 4) is somewhat arbitrary and probably not optimal. Nevertheless, it divides the beam profile into a region close to the main beam, an intermediate region, and a region very far from the beam axis, with little overlap between the regions, which physically makes sense. This can, in particular, be used to plan the ground calibration

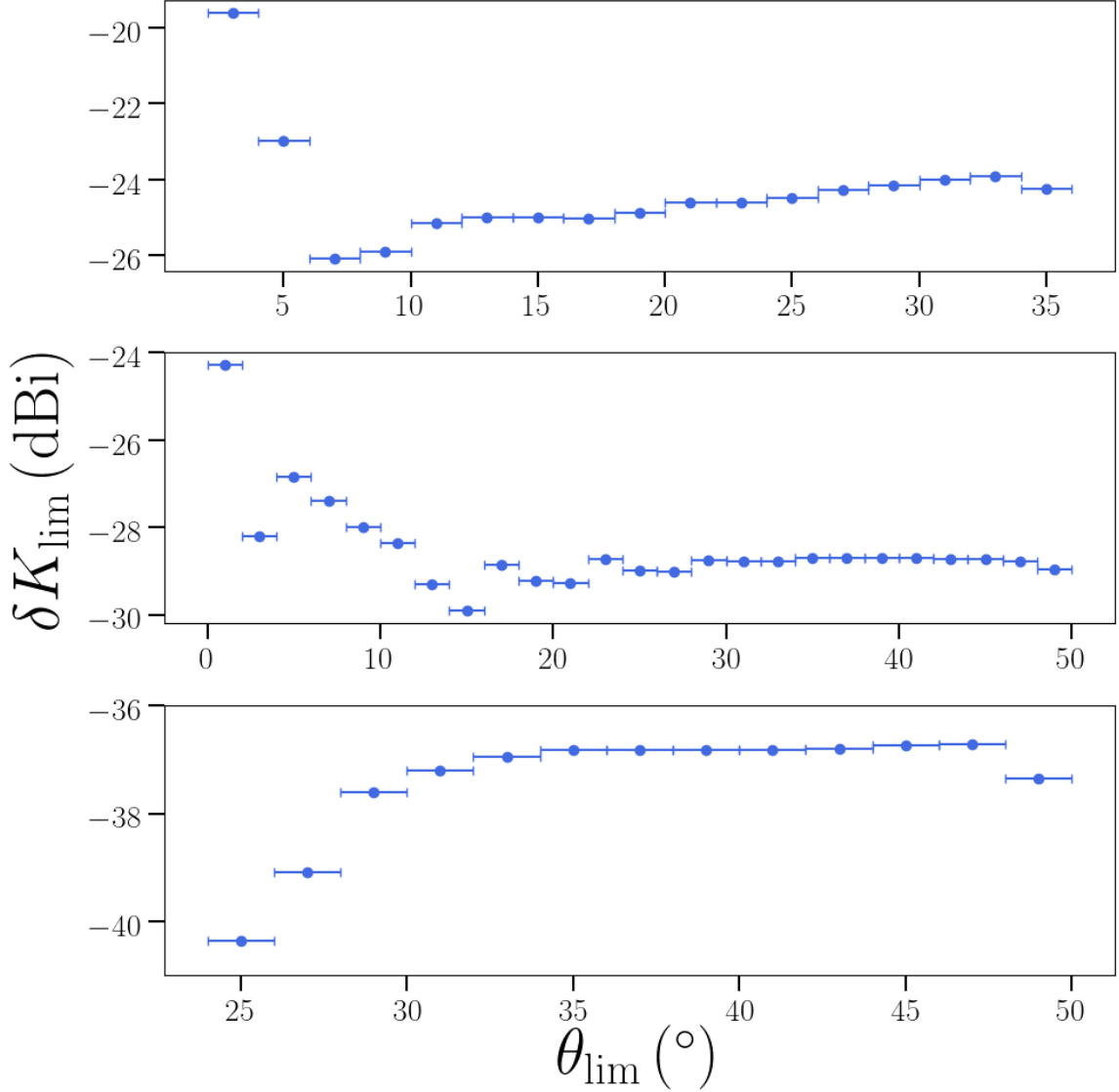


Figure 16: Values of δK_{lim} for which $\delta r = \delta r_{\text{lim}}$ as a function of θ_{lim} , in units of the total beam integral, at 40 GHz (top), 140 GHz (middle) and 402 GHz (low). These are computed for values of b such that the integral in δK_{lim} is positive and for values of $\theta_{\text{lim}} \leq \theta_{\text{lim}} (\delta r = \delta r_{\text{lim}}, b = 0)$.

strategy by dividing the beam into regions that can be calibrated with different accuracies. The definition of the windows lead to an apparent inconsistency where two very different requirements are defined at a same angle in the overlap region of two windows. This can be solved by defining a smooth error curve based on the requirements, see Section 5.5. In addition, it will be possible to tune the accuracy in the different regions by tuning the resolution of the measurements, contrary to what we did here assuming constant resolution of 0.25 deg^2 . Perturbations in more angular windows will be simulated in future studies, allowing to define requirements with a better angular resolution as well as a more thorough inspection of the effect of these perturbation windows.

In addition, these windows are completely axisymmetric, as well as the quantities $\delta \bar{B}_{\text{lim}}$, $\delta \bar{R}_{\text{lim}}$ and σ_{calib} , which could be the source of an inconsistency in the results because the beams used to

$\delta B_{\text{lim}} \text{ (dB)} - \delta B_{\text{lim}}^{\text{const}} \text{ (dB)}$											
ν (GHz)	LFT										
	40	50	60	68		78		89		100	119
$4^\circ < \theta < 8^\circ$	-1.25	-1.23	-1.06	-0.97	0.11	-1.86	-1.84	-2.08	-1.96	-2.34	-2.75
$7^\circ < \theta < 12^\circ$	-1.47	-1.11	-1.26	-1.22	-0.56	-2.10	-2.08	-2.30	-2.16	-2.53	-2.90
$11^\circ < \theta < 70^\circ$	-0.57	2.46	-0.53	0.15	0.66	-2.53	-2.95	-4.07	-4.32	-3.22	-0.35
ν (GHz)	LFT	MFT					HFT				
	140	100	119	140	166	195	195	235	280	337	402
$4^\circ < \theta < 8^\circ$	-3.97	-1.93	-2.36	-3.55	-1.65	-1.93	-1.34	-1.82	-2.76	-2.85	-3.14
$7^\circ < \theta < 12^\circ$	-3.32	-2.18	-2.61	-2.93	-1.84	-1.97	-1.72	-2.00	-2.97	-3.03	-3.25
$11^\circ < \theta < 70^\circ$	3.22	-1.21	0.95	1.22	0.19	-0.61	-2.50	-3.26	3.29	-1.22	-0.07

Table 7: δB_{lim} using perturbations with constant δB and with the fiducial shape in standard method for each frequency channel and each of the three angle ranges of the beam perturbations giving $\Delta r_{\text{FSL}} = 1.9 \times 10^{-5}/66$.

produce the simulations include some asymmetries, even if not at a realistic level. However, the comparison performed in Section 4.2.1 teaches us that the results are, to some extent, robust. This correspondence between a fully symmetric case and a case that includes some level of asymmetries could come from the combination of many symmetrically distributed detectors on the focal plane and from the symmetrizing effect of the scanning strategy, optimized to observe the same pixels from many different angles.

5.2 Requirements on modelisation

As explained in Section 3.1.2, we chose the power law beam model to reproduce the main falling tail feature of beam profiles while staying rather general and simple. From its generality, we expect our results to be rather independent of this particular modeling. Indeed, we saw that we could describe the bias on r using a simple physical characteristic of the imperfect beam knowledge, δK_{lim} , which is completely independent both of the reference GRASP beams and of the power law model. Therefore, we are confident that the results from this section are general and apply to a large variety of cases.

After some sufficiently large angle θ_{lim} , depending on the frequency channel, the effect of beam mismodeling corresponds to a modification of the signal at large scales. After calibrating on the dipole, this will have a net effect of scaling the normalisation of the multipoles $ell \geq 2$, introducing a bias proportional to the square of this change of normalisation, i.e. to $(\delta K_{\text{lim}})^2$. This regime only occurs for angles larger than some transition θ_{lim} because for lower angles, the effect of the beam miscorrection is quite different. It acts at smaller scales which, after dipole, calibration will affect higher multipole. This is a potentially promising finding. Indeed, if we manage to measure the residual power in the far side-lobes region at $\theta > \theta_{\text{lim}}$ with a precision better than δK_{lim} , then we would be able to mitigate completely the systematic effect from beam far side-lobes. However, it does not look straightforward to measure the integrated power of the beam on such a large angular range, so this will require some sophisticated methods to calibrate this parameter in the context of the *LiteBIRD* mission, possibly at the data analysis level including the δK_{lim} parameter in the component separation method.

5.3 Limitations, assumptions and future improvements

Because of the complexity of the present work, putting together multiple steps of the forecasting pipeline together, all undergoing active research, we had to face technical limitations as well as make key methodological assumptions to obtain the results described in Section 4. In particular, by refining the optical modeling or and the sky convolution, or by changing the data analysis pipeline (in particular the component separation stage), the requirements on the level of accuracy of beam

measurements can potentially change by orders of magnitude and should, thus, be understood as the set of requirements obtained in the given context described here. For completeness, we detail in the following some of our assumptions that will need to be improved or further explored in future studies.

The beam models used for the above far side-lobes study are obtained from a **GRASP** simulation assuming ideal optical systems. In particular, the external satellite geometry such as the presence of fore-baffles and V-grooves for which we expect reflection and diffraction to occur is not taken into account, significantly modifying the reference beam shapes. This would have a positive effect on the requirements by lowering the amplitude of the far side-lobes, possibly reducing the relevant size of the last angular window (see Figure 10). In the optical system itself, no cross-polar contribution to the beam is taken into account in this study. We expect the cross-polar contribution to be reduced by the HWP, but it was shown in [32] that high level of cross-polar contributions in the presence of a HWP are possible, and no effect from the HWP beyond the modulation of the polarization signal is included in the simulations of LiteBIRD either. Thus, the impact of the interactions between cross-polar beams and the HWP will need to be addressed in the future. As far as only the error on the transfer function is concerned, as we shall see in the next sections, it appears that our analyses are fairly independent of the particular beam shapes. Thus, the results of the previous sections would still be valid even when more realistic beam simulations are available, given the stability of δR_{lim} and δK_{lim} .

Furthermore, because the simulated optical system is incomplete, the beam asymmetries are underestimated, especially for detectors on the edge of the focal planes. Enhanced asymmetries could lead to an additional contribution to the bias. The induced leakage from E modes to B modes should, nevertheless, still be mitigated by the HWP in absence of instrumental polarization, generated by diffraction on the V-grooves for instance. Therefore, all our results assume implicitly that the averaging over detectors in a given frequency channel and the scanning strategy of *LiteBIRD* induce enough symmetrization of the effective beams, in contrast with the very asymmetric beams of the Planck satellite [16]. The comparison between our two methods detailed in Section 4.2.1, where one includes the current level of asymmetries but the other does not, tends to show that this is indeed the case for the incomplete beam simulations we have at hands.

Finally, throughout this work, our goal was to study and isolate the effect of beam far side-lobes mismatch on the cosmological results. Therefore, we did not take into account other potential sources of errors nor their interplay with far side-lobes systematic effects. In particular, we used a very simple spatially homogeneous foreground model that may not be realistic since evidence for spatial variations of the SEDs was found in Planck data [35]. However, first of all, we expect our analysis to be reliable despite the simple foreground model because we always compare the residuals including effects from imperfect beam knowledge with residuals from a reference case (see equation Eq. (3.24)). However, it is expected that the results depend significantly on the particular component separation method that we used here. Because our method of foreground cleaning is parametric without any mitigation procedure and the impact of the beam far side-lobes is to modify the polarization frequency maps normalization factor from the dipole calibration procedure and effectively change the observed SEDs of the polarized foreground components, our approach will be particularly sensitive to this effect. Other methods, such as blind methods, are in principle more flexible and should be able to compensate this effect, to some extent. Therefore, we can expect the requirements to be significantly relaxed by using a blind component separation method. An equivalent approach to relax the requirements presented in this paper would be to modify the parametric component separation approach with a mitigation procedure of the far side-lobes effect, taking into account the error on the dipole calibration factor due to the far side-lobe mismatch, which is left for future work. As we see, considering the dipole calibration step is crucial to understand the impact of far side-lobes. Here, we assumed it to be perfect, however in a more realistic setting there will be errors and miscalibration having an unknown impact on beam far side-lobes systematic effects. The study of these interplays is, again, left for future work.

5.4 Application to a realistic physical effect: Ruze’s lobes

As an example of how the derivation of requirements described in this work can be used in the presence of a realistic physical effect, we consider the case of Ruze’s lobes. Note that, we do not present here a realistic study of the impact of the Ruze’s lobes effect, but show how the formalism developed in this work could be used for such a study.

As described in his seminal paper [41], the effect of irregular optical surface (e.g. reflectors, lenses, etc.) on the beam profile can be modeled by introducing a random phase to the signal. It leads to an exponentially suppressed redistribution of the power from the main beam towards regions at higher angle, following:

$$B^{\text{Ruze}}(\theta) = e^{-\overline{\delta^2}} \left[\overline{B_0}(\theta) + \left(\frac{2\pi c}{\lambda} \right)^2 \sum_{n=1}^{+\infty} \frac{(\overline{\delta^2})^n}{n \cdot n!} e^{-(\pi c \sin(\theta)/\lambda)^2/n} \right], \quad (5.2)$$

where c is the defect correlation length, i.e. radius of the typical defect, λ the wavelength and $\overline{\delta^2}$ the phase front variance at the origin of the effect. This variance can be expressed in terms of the RMS surface error ϵ , i.e. the size of the typical surface irregularities:

$$\overline{\delta^2} = \left(\frac{4\pi\epsilon}{\lambda} \right)^2. \quad (5.3)$$

In this exercise, we truncate the infinite sum, keeping only the terms for $n \leq 10$, and for a given frequency we are left with the set of two free parameters (c, ϵ). Figure 17 illustrates the impact on the beam profile for multiple values of the parameters in the *LiteBIRD*’s 100 GHz LFT channel. In order to be comparable with the types of perturbations considered in this paper, we choose to investigate the case where the parameters are ($c = 1.2$ cm, $\epsilon = 5$ μ m), which affects the angular range spanned by the two first windows. Note, however, that this model also induces a deformation of the main beam and near side-lobes, which we neglect here for the purpose of the exercise, as we are illustrating how the formalism developed in the context of the far side-lobes can be used. We know that the important parameter to consider is δR_{lim} which in this case is:

$$\delta R_{\text{lim}}^{\text{Ruze}} = \frac{\int [B^{\text{Ruze}}(\theta) - \overline{B_0}(\theta)] W(\theta) d\Omega}{\int \overline{B_0}(\theta) d\Omega}. \quad (5.4)$$

We find that $\delta R_{\text{lim}}^{\text{Ruze}} = -27.68$ dB in the first window and $\delta R_{\text{lim}}^{\text{Ruze}} = -34.06$ dB in the second, to be compared with the requirements in Table 3. Being below the requirements in the two windows, we would conclude that such characteristics for the surface irregularities are compatible with the requirements on the beam far side-lobes to achieve the scientific goal of the mission.

5.5 Linking requirements to reconstructed beam error bars

In this section, we explore how the requirements on δB_{lim} defined in Table 4 can be translated in terms of error bars on the beam reconstruction. For illustration purposes, we start from an arbitrary symmetrized “theoretical beam”, whose profile is shown in red in the upper panel of Fig. 18, for $\theta > 0$. For concreteness, we assume that the beams will be reconstructed by a combination of measurements (ground calibration campaign) and optical modeling. As both the measurements and the simulations are subject to systematic errors (for example quality of the quiet zone on one side, and the precision of the optical model used as inputs for GRASP simulations on the other), we consider that the reconstructed beam will come together with a level of systematic error. This error typically comes from a residuals between model and measurements. We consider that the requirements apply to this systematic error and depend on the beam amplitude.

In Fig. 18, the black curve is the reconstructed beam assuming the systematic residual between the measurement and the theoretical beam which is illustrated on the figure of the left panel. We also indicate the $\delta B_{\text{lim}}^{\nu, W}$ values corresponding to the difference between the black and the red curves

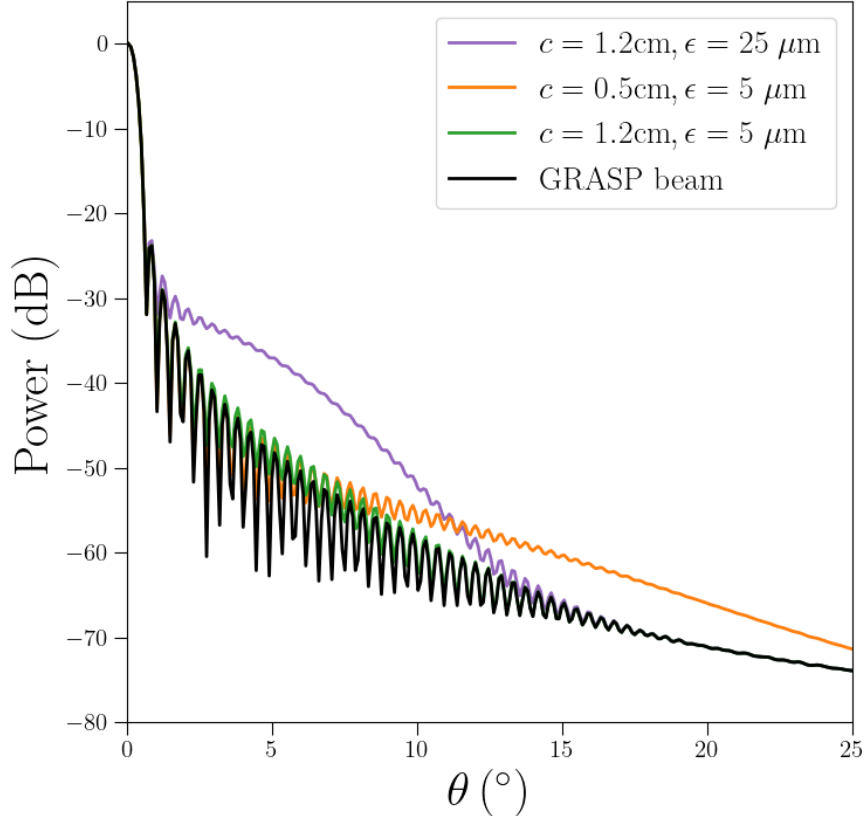


Figure 17: Illustration of the impact of surface irregularities in the optical system on the shape of the beam profile, following the model Eq. (5.4) for different set of parameters, in *LiteBIRD*'s 100 GHz LFT channel.

(the reconstructed beam amplitude is assumed to be zero above 60 degrees). The curve of systematic residuals is found by a trial-and-error approach to match approximately the corresponding δB_{lim} values to those of the Table 4, for the MFT 166 GHz channel. This is achieved for a residual error of $\simeq 3$ dB at -60 dB and 7 dB at -80 dB, ie the order of magnitude that has been achieved on the Planck RFQM at 100 GHz. Contrary to the requirements on δB_{lim} that depend on the beam shape only through the size of the angular window, this smooth error curve dramatically depends on the theoretical beam shape.

6 Conclusion

Instrument calibration is a critical step to mitigate systematic effects and define the instrument model necessary to perform a correct data analysis. We have studied the impact of beam far side-lobes through a simple procedure of beam perturbation in simulated observations. As a demonstration of the reliability of the framework, we set requirements on the calibration of beam amplitudes, under a set of assumption on the instrument, the analysis methods and mission choices, in three angular windows ranging from regions near the main beam up to 70° which we related to physical quantities. We compared a procedure including a simulation of the focal plane and of the scanning strategy of *LiteBIRD* with a simpler method including only axisymmetric beams and direct convolution of

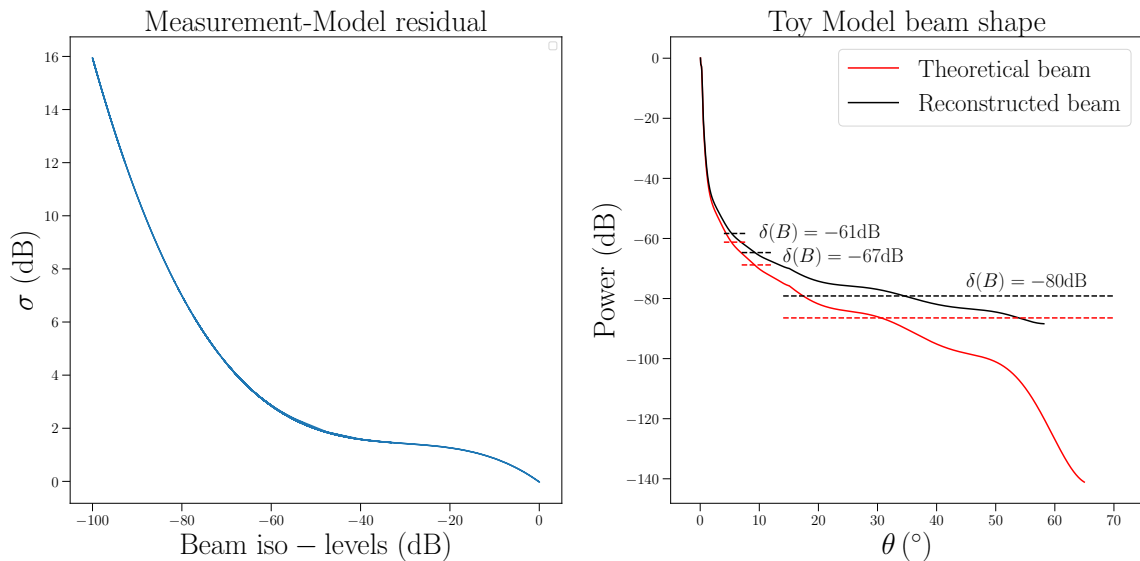


Figure 18: Left: Illustration of assumed systematic residuals between model and measurements found by trial-and-error to match approximately the requirements of Table 4 for the MFT 166 GHz channel. Right: Illustration of an arbitrary theoretical beam shape (in red) together with the reconstructed one (in black) assuming the systematic residuals between this model and measurements given by the figure of the left panel.

the sky signal and found the results to be comparable which allowed us to use the latter, a much simpler and faster method. Far from the main beam, we have found that the relevant parameter to be constrained is the difference of power in the far side-lobes between the model and the actual beam, regardless of the beam shape. Provided this parameter can be measured this could open a window to mitigate the beam far side-lobes systematic effect without having to rely too much on modeling in regions very far from the beam axis.

7 Acknowledgements

LiteBIRD (phase A) activities are supported by the following funding agencies: ISAS/JAXA, MEXT, JSPS, KEK (Japan); CSA (Canada); CNES, CNRS, CEA (France); DFG (Germany); ASI, INFN, INAF (Italy); RCN (Norway); AEI (Spain); SNSA, SRC (Sweden); NASA, DOE (USA). JE acknowledges the SciPol project funded by the European Research Council (ERC) under the European Union’s Horizon 2020 research and innovation program (Grant agreement No. 101044073). JEG acknowledge support from the Swedish National Space Agency (SNSA/Rymdstyrelsen) and the Swedish Research Council (Reg. no. 2019-03959). JEG also acknowledges support from the European Union (ERC, CMBeam, 101040169). The work of TM was supported by JSPS KAKENHI Grant Number 23H00107.

References

- [1] C. L. Bennett, A. Banday, K. M. Gorski, G. Hinshaw, P. Jackson, P. Keegstra et al., *Four year COBE DMR cosmic microwave background observations: Maps and basic results*, *Astrophys. J. Lett.* **464** (1996) L1 [[astro-ph/9601067](#)].
- [2] G. Hinshaw, D. Larson, E. Komatsu, D. N. Spergel, C. L. Bennett, J. Dunkley et al., *Nine-year wilkinson microwave anisotropy probe (wmap) observations: Cosmological parameter results*, *The Astrophysical Journal Supplement Series* **208** (2013) 19.

- [3] PLANCK collaboration, N. Aghanim et al., *Planck 2018 results. I. Overview and the cosmological legacy of Planck*, *Astron. Astrophys.* **641** (2020) A1 [1807.06205].
- [4] A. H. Guth, *The Inflationary Universe: A Possible Solution to the Horizon and Flatness Problems*, *Phys. Rev. D* **23** (1981) 347.
- [5] A. D. Linde, *A New Inflationary Universe Scenario: A Possible Solution of the Horizon, Flatness, Homogeneity, Isotropy and Primordial Monopole Problems*, *Phys. Lett. B* **108** (1982) 389.
- [6] M. Kamionkowski, A. Kosowsky and A. Stebbins, *Statistics of cosmic microwave background polarization*, *Phys. Rev. D* **55** (1997) 7368 [astro-ph/9611125].
- [7] M. Zaldarriaga and U. Seljak, *An all sky analysis of polarization in the microwave background*, *Phys. Rev. D* **55** (1997) 1830 [astro-ph/9609170].
- [8] D. Chowdhury, J. Martin, C. Ringeval and V. Vennin, *Assessing the scientific status of inflation after Planck*, *Phys. Rev. D* **100** (2019) 083537 [1902.03951].
- [9] M. Tristram et al., *Improved limits on the tensor-to-scalar ratio using BICEP and Planck*, [2112.07961](#).
- [10] G. Franco, P. Fosalba and J. A. Tauber, *Systematic effects in the measurement of polarization by the PLANCK telescope*, *Astron. Astrophys.* **405** (2003) 349 [astro-ph/0210109].
- [11] C. Burigana, M. Sandri, F. Villa, D. Maino, R. Paladini, C. Baccigalupi et al., *Trade - off between angular resolution and straylight contamination in CMB anisotropy experiments. 2. Straylight evaluation*, *Astron. Astrophys.* **428** (2004) 311 [astro-ph/0303645].
- [12] K. M. Huffenberger, B. P. Crill, A. E. Lange, K. M. Górski and C. R. Lawrence, *Measuring Planck beams with planets*, *Astron. Astrophys.* **510** (2010) A58 [1007.3468].
- [13] P. A. Gallardo, N. F. Cothard, R. Puddu, R. Dünner, B. J. Koopman, M. D. Niemack et al., *Far Sidelobes from Baffles and Telescope Support Structures in the Atacama Cosmology Telescope*, **8**, 2018, [1808.05101](#), DOI.
- [14] LITEBIRD collaboration, A. T. Lee et al., *LiteBIRD: an all-sky cosmic microwave background probe of inflation*, in *Bulletin of the American Astronomical Society*, vol. 51, p. 286, Sept., 2019.
- [15] LITEBIRD collaboration, E. Allys et al., *Probing Cosmic Inflation with the LiteBIRD Cosmic Microwave Background Polarization Survey*, *Progress of Theoretical and Experimental Physics* (2022) .
- [16] Planck Collaboration, *Planck 2015 results. VII. High Frequency Instrument data processing: Time-ordered information and beams*, *Astron. Astrophys.* **594** (2016) A7 [1502.01586].
- [17] E. Hivon, S. Mottet and N. Ponthieu, *QuickPol: Fast calculation of effective beam matrices for CMB polarization*, *Astron. Astrophys.* **598** (2017) A25 [1608.08833].
- [18] M. Lungu et al., *The Atacama Cosmology Telescope: Measurement and Analysis of 1D Beams for DR4*, [2112.12226](#).
- [19] S. Mitra, G. Rocha, K. M. Gorski, K. M. Huffenberger, H. K. Eriksen, M. A. J. Ashdown et al., *Fast Pixel Space Convolution for CMB Surveys with Asymmetric Beams and Complex Scan Strategies: FEBeCoP*, *Astrophys. J. Suppl.* **193** (2011) 5 [1005.1929].
- [20] LITEBIRD collaboration, Y. Sekimoto et al., *Concept Design of Low Frequency Telescope for CMB B-mode Polarization satellite LiteBIRD*, *Proc. SPIE Int. Soc. Opt. Eng.* **11453** (2020) 1145310 [2101.06342].
- [21] LITEBIRD collaboration, L. Montier et al., *Overview of the Medium and High Frequency Telescopes of the LiteBIRD satellite mission*, *Proc. SPIE Int. Soc. Opt. Eng.* **11443** (2020) 114432G [2102.00809].
- [22] LITEBIRD collaboration, M. Hazumi et al., *LiteBIRD: JAXA's new strategic L-class mission for all-sky surveys of cosmic microwave background polarization*, *Proc. SPIE Int. Soc. Opt. Eng.* **11443** (2020) 114432F [2101.12449].
- [23] R. S. Hill et al., *Five-Year Wilkinson Microwave Anisotropy Probe Observations: Beam Maps and Window Functions*, *The Astrophysical Journal Supplement* **180** (2009) 246 [0803.0570].
- [24] Planck Collaboration, *Planck 2015 results. IV. Low Frequency Instrument beams and window functions*, *Astron. Astrophys.* **594** (2016) A4 [1502.01584].

- [25] “GRASP10.” <https://www.ticra.com/software/grasp/>.
- [26] B. Thorne, J. Dunkley, D. Alonso and S. Naess, *The Python Sky Model: software for simulating the Galactic microwave sky*, *Mon. Not. Roy. Astron. Soc.* **469** (2017) 2821 [1608.02841].
- [27] Z. Li, G. Puglisi, M. S. Madhavacheril and M. A. Alvarez, *Simulated catalogs and maps of radio galaxies at millimeter wavelengths in Websky*, **2110.15357**.
- [28] G. Puglisi, V. Galluzzi, L. Bonavera, J. Gonzalez-Nuevo, A. Lapi, M. Massardi et al., *Forecasting the Contribution of Polarized Extragalactic Radio Sources in CMB Observations*, *Astrophys. J.* **858** (2018) 85 [1712.09639].
- [29] “TOAST.” <https://github.com/hpc4cmb/toast>.
- [30] G. Prézeau and M. Reinecke, *Algorithm for the evaluation of reduced wigner matrices*, *The Astrophysical Journal Supplement Series* **190** (2010) 267–274.
- [31] A. J. Duivenvoorden, J. E. Gudmundsson and A. S. Rahlin, *Full-Sky Beam Convolution for Cosmic Microwave Background Applications*, *Mon. Not. Roy. Astron. Soc.* **486** (2019) 5448 [1809.05034].
- [32] A. J. Duivenvoorden, A. E. Adler, M. Billi, N. Dachlythra and J. E. Gudmundsson, *Probing frequency-dependent half-wave plate systematics for cmb experiments with full-sky beam convolution simulations*, *Monthly Notices of the Royal Astronomical Society* **502** (2021) 4526–4539.
- [33] T. Ghigna, T. Matsumura, G. Patanchon, H. Ishino and M. Hazumi, *Requirements for future CMB satellite missions: photometric and band-pass response calibration*, *JCAP* **11** (2020) 030 [2004.11601].
- [34] P. Collaboration, “The Planck Legacy Archive.” <https://pla.esac.esa.int>.
- [35] PLANCK collaboration, Y. Akrami et al., *WavePlanck 2018 results. IV. Diffuse component separation*, *Astron. Astrophys.* **641** (2020) A4 [1807.06208].
- [36] N. Krachmalnicoff, C. Baccigalupi, J. Aumont, M. Bersanelli and A. Mennella, *Characterization of foreground emission on degree angular scales for CMB B-mode observations - Thermal dust and synchrotron signal from Planck and WMAP data*, *Astron. Astrophys.* **588** (2016) A65 [1511.00532].
- [37] J. Errard, S. M. Feeney, H. V. Peiris and A. H. Jaffe, *Robust forecasts on fundamental physics from the foreground-obscured, gravitationally-lensed CMB polarization*, *JCAP* **03** (2016) 052 [1509.06770].
- [38] R. Stompor, S. M. Leach, F. Stivoli and C. Baccigalupi, *Maximum Likelihood algorithm for parametric component separation in CMB experiments*, *Mon. Not. Roy. Astron. Soc.* **392** (2009) 216 [0804.2645].
- [39] R. Stompor, J. Errard and D. Poletti, *Forecasting performance of CMB experiments in the presence of complex foreground contaminations*, *Phys. Rev. D* **94** (2016) 083526 [1609.03807].
- [40] D. Dubruel, “Planck RFQM Evaluation Report.” Thales Alenia Space ref.:H-P-3-ASP-TR-1144, Issue 5, 2008.
- [41] J. Ruze, *Antenna tolerance theory—a review*, *Proceedings of the IEEE* **54** (1966) 633.

A Correction by the effective beam

Individual effective beams are produced in each frequency channel and for each Stokes parameter. We do not use the simulated beams at the detector level to produce the effective beams because these are transformed in a highly non-trivial way by the scanning strategy and map-making. So, we compute the effective beams by directly comparing the power spectra from the band-pass integrated PySM sky emission maps as reference and the unperturbed $\mathbf{m}_{4\pi}^\nu$ maps. The transfer functions in harmonic domain is, thus, given by:

$$b_{\ell,\text{eff}} = \sqrt{\frac{C_\ell^{\text{ref}}}{C_\ell^{4\pi}}}, \quad (\text{A.1})$$

that we decided to fit (A.1) with an empirical function $\beta_\ell(\lambda, \mu_i) = P_\ell^3(\mu_i) e^{-\ell^2/\lambda}$, where P_ℓ^3 is a third order polynomial in ℓ with parameters μ_i .

We apply beam deconvolution per frequency by translating input maps into harmonic domain, using their $\mathbf{a}_{\ell m}$ coefficients instead of pixel amplitudes. The beam corrected input signal is therefore:

$$\mathbf{a}_{\ell m, \text{corr}}^\nu = \frac{\mathbf{a}_{\ell m, \text{pert}}^\nu}{b_{\ell, \text{eff}}^\nu}. \quad (\text{A.2})$$